

High-Precision Approximation of Riemann Zeros via the Truncated Weil Form

Akiva Groskin

May 2026

MSC 2020: 11M26 (primary), 65F15, 65N25 (secondary).

Keywords: Riemann zeta function, Weil quadratic form, Connes–van Suijlekom truncation, Galerkin method, Sobolev regularity, Dirichlet L -functions, arbitrary-precision computation, independent reproduction.

Abstract

The Connes–van Suijlekom truncated Weil quadratic form, indexed by a cutoff parameter c that controls the primes $p \leq c$ entering the operator, produces a ground state whose Fourier–Mellin zeros provably lie on the critical line; whether they converge to the Riemann zeros as $c \rightarrow \infty$ is open (Connes 2026; Connes–Consani–Moscovici 2025). We present, to our knowledge, the first independent public implementation of the Connes–van Suijlekom Galerkin matrix at sixteen cutoffs ($c = 13$ through 67, plus $c = 100$). Across the in-sample window $c = 13$ through $c = 67$ at $N = 100$, the first-zero absolute error $|\gamma_1 - \gamma_1^{\text{Riemann}}|$ shrinks monotonically from $\sim 2 \times 10^{-55}$ to $\sim 1.5 \times 10^{-168}$ — a 113-OOM convergence across fifteen cutoffs (Table 3). The smallest-positive even-sector eigenvalue $\lambda_{\min}^{\text{even}}$ separately reaches $\sim 10^{-334}$ at $c = 100$, $N = 250$ (275-OOM span from $c = 13$).

Out-of-sample test at $c = 100$. On the four-point N -sweep $N \in \{100, 150, 200, 250\}$ at $\text{dps} = 500$, consecutive first-difference ratios 0.837 and 0.836 match to two decimal places. Aitken- Δ^2 on the two overlapping triples yields $\log_{10} |\lambda_{\infty}^{\text{even}}| \approx -536.8$ and ≈ -533.7 , approaching the Connes 2026 §6.4 heuristic prediction (≈ -530.4) monotonically with N (6.4 and 3.3 OOM gaps out of $|x_{\infty}| \sim 530$). The same eigenvector recovers $\gamma_1, \dots, \gamma_{10}$ to 307–329 matching digits at $N = 250$, $\text{dps} = 500$. Under the unitary equivalence with Connes–Consani–Moscovici Lemma 5.1, this is the deepest such Galerkin-truncation recovery in the public Connes–van Suijlekom/Connes–Consani–Moscovici literature, subject to a hypothesis-status caveat: the raw finite- N matrix carries a small block of dps-stable negative-sign eigenvalues, so we report the *smallest-positive* branch (continuum positivity of QW_{λ} is RH-equivalent and is not assumed at $\lambda = \sqrt{100}$). The fit $|\log_{10} \lambda_{\min}| \approx 13.24 c^{0.634}$ on $c \leq 67$ at $N = 100$ is shown to be a finite- N rate, falsified at $c = 100$, $N = 200$ by 49 OOM in the direction of faster decay.

Structural observations include approximate eigenvector c -invariance (overlap ≥ 0.9498 on all 105 cutoff pairs despite eigenvalues differing by 113 OOM), multi-zero convergence universality (all ten detectable zeros within 3.8% of each other), an empirical Galerkin-convergence exponent $s(c) \approx 55 \log c - 128$, un-rescaled Galerkin bulk-spectrum Poisson statistics ($\beta < 0.05$; this is a structural diagnostic of the truncated operator, not a test of Montgomery’s conjecture, which applies to locally-rescaled zero spacings), and tight bulk invariants $\log |\det Q_c| \approx -65.6 c + 542$ ($R^2 = 0.997$).

We make no claim of proof; the contribution is reproducible numerical data and its careful interpretation under the existing CvS/CCM framework.

All code, data, and ancillary files are publicly available.

1 Introduction

In February 2026, Connes published “Past, Present and a Letter Through Time” [4], revisiting the spectral interpretation of the Riemann zeros within the framework of noncommutative geometry. Section 6 of that paper presents what is, in effect, an open question: for each value of a cutoff parameter c (controlling the primes $p \leq c$ entering the operator; c itself need not be prime), the truncated Weil quadratic form on $L^2([0, \log c])$ admits a unique even-sector ground state whose Fourier–Mellin zeros provably lie on the critical line. Do these zeros converge to the actual Riemann zeros as $c \rightarrow \infty$?

The criticality statement is a theorem. Connes–van Suijlekom [9] establish (Theorem 6.1) that the zeros of $\hat{\eta}_c$ are real for every finite c , so the open question is specifically about convergence, not about criticality. If the convergence holds, RH follows by Hurwitz’s theorem applied to the Mellin transforms — but the convergence itself is unproven.

Connes reports numerical data for the first fifty zeros at $c = 13$, with errors ranging from approximately 2.6×10^{-55} (first zero) to approximately 10^{-3} (fiftieth zero); the first-zero error relative to $\gamma_1 = 14.134725\dots$ is the datum reproduced in this work. Connes–Consani–Moscovici [8] report the related number 2.44×10^{-55} at the same cutoff, with $N = 120$ and 200-digit precision. As of April 2026, no independent public reproduction of these numbers exists. No public code implementing the Connes–van Suijlekom Galerkin matrix has been located in a literature sweep encompassing arXiv, GitHub, MathOverflow, and seminar recordings (see Section 9).

Contributions

This paper makes five primary contributions:

- 1. Independent reproduction and extension.** We provide, to our knowledge, the first public implementation of the Connes–van Suijlekom Proposition 4.1 Galerkin matrix (Python/mpmath); reproduce the $c = 13$ first-zero error within a factor of 1.3 of the value reported by Connes 2026; cross-validate against Connes–Consani–Moscovici at $c = 14$; and extend the measurements to fifteen cutoffs ($c = 13$ through 67) spanning 113 orders of magnitude in $|\gamma_1 \text{ error}|$, plus a sixteenth cutoff at $c = 100$.
- 2. Out-of-sample empirical test of Connes 2026 §6.4 at $c = 100$.** At $c = 100$ we measure $\log_{10} |\lambda_{\min}^{\text{even}}|$ on a four-point N -sweep $N \in \{100, 150, 200, 250\}$ at $\text{dps} = 500$ (with a $\text{dps} = 1000$ retest at $N = 150$), with values $-190.92, -247.19, -294.31, -333.68$. The consecutive first-difference ratios 0.8373 and 0.8355 match to two decimal places, evidence for a local geometric model of the convergence sequence. Aitken- Δ^2 applied to the two consecutive overlapping triples gives $\log_{10} |\lambda_{\infty}^{\text{even}}(c = 100)| \approx -536.76$ (from $\{100, 150, 200\}$) and ≈ -533.70 (from $\{150, 200, 250\}$); the Connes 2026 §6.4 heuristic continuum prediction is ≈ -530.38 , giving gaps of 6.39 and 3.32 orders of magnitude respectively, out-of-sample (the in-sample fit window was $c \leq 67$). Section 6 presents the computation.
- 3. Recognition that the numerical pipeline measures the Connes–Consani–Moscovici operator’s spectrum.** Under the unitary equivalence established in §2.4 with Connes–Consani–Moscovici (2025) Lemma 5.1, our F_{even} test function is, up to a positive scaling constant, the Fourier–Mellin transform $\hat{\xi}_N(z)$ appearing in Connes–Consani–Moscovici Theorem 1.1(iii); we recognize — we do not claim to discover — that our extracted zeros are, modulo the hypothesis status at $c = 100$ (Remark 2.1), eigenvalues of the Connes–Consani–Moscovici rank-one operator $D_{\log}^{(\lambda, N)}$ at $\lambda = \sqrt{c}$. This makes our fifteen-cutoff sweep plus

the $c = 100$ datum, to our knowledge, the first independent multi- c survey of that spectrum at trigonometric-Galerkin matching-digit precision, beyond Connes–Consani–Moscovici’s own reported values at $c \in \{9, 12, 13, 14\}$; the deepest γ_1 extraction at $c = 100$ reaches 329 matching digits at $N = 250$, $\text{dps} = 500$.

4. **Structural characterization of the finite- N operator.** We identify quantitative properties that constrain theoretical work: (a) the Sobolev regularity scales as $s(c) \approx 55 \cdot \log c - 128$ at six cutoffs; (b) all ten detectable zeros converge at rates within 3.8% of each other; (c) the eigenvector is approximately c -invariant (> 0.950 overlap across all 105 pairs); (d) the normalized zero-crossing shape varies by only 3.3%; (e) interval extension, not prime identity, drives convergence ($r = -0.96$); (f) the spectral trace decays as $c^{-0.116}$ while the Frobenius norm is constant; (g) the bulk spectrum is Poisson (no level repulsion); (h) nine convergence models fail (Section 5); (i) the empirical $|\log_{10} \lambda| \approx 13.24 c^{0.634}$ fit is a finite- $N = 100$ rate, not the continuum asymptote, falsified at $c = 100$, $N = 200$ by 49 OOM and corroborated by a $c = 67$, $N = 150$ rerun showing a 46 OOM drop versus the same- c , $N = 100$ datum; (j) five negative-sign eigenvalues at $c = 100$, $N = 150$ reproduce identically across $\text{dps} \in \{500, 1000\}$, showing they are not simple working-precision noise; a plausible explanation is condition-driven sign loss in the finite- N truncation, still requiring certification.
5. **Partial extension to Dirichlet L -functions.** A port to $L(s, \chi_3)$ converges at $c = 13, 17, 37$ (16–28 digits) but exhibits an oscillating positivity breakdown at $c = 23, 29$, revealing a structural dependence on the character that is absent in the zeta case.

Explicit non-claims

We do not claim to validate Connes’ convergence conjecture. We do not claim a proof of the Riemann Hypothesis. We do not claim that the Aitken extrapolation at $c = 100$ proves a convergence rate. The agreement at $c = 13$ is a consistency check against published values, not a comparison against an independent prediction. The agreement at $c = 100$ between our Aitken extrapolation and the Connes 2026 §6.4 prediction is an empirical consistency test, not a theorem; we are explicit that Aitken acceleration carries assumptions about the local form of the convergence sequence, and the Connes 2026 §6.4 prediction is itself a heuristic statement based on the agreement (their Figure 1) between $1 - \chi_2(\lambda)$ and $\varepsilon(\lambda)$ on $\lambda \leq 14$. We report the agreement; we do not promote it.

2 Mathematical Setup

2.1 The Weil quadratic form and its truncation

We follow the notation of Connes–van Suijlekom [9] and Connes–Consani [5]. For a cutoff parameter c (controlling the primes $p \leq c$ in the prime-sum piece below; c itself need not be prime, as in our $c = 14$ and $c = 100$ cells), set $L = \log c$. The quadratic form acts on $L^2([0, L])$ and decomposes as

$$D = D_\infty + D_{\text{pole}} + D_{\text{prime}}, \tag{1}$$

where D_∞ is the archimedean contribution, D_{pole} is the pole contribution from the zeta function, and D_{prime} sums over primes $p \leq c$.

The archimedean Mellin multiplier is

$$h_+(\tau) = -\log \pi + \text{Re} \Psi\left(\frac{1}{4} + \frac{i\tau}{2}\right), \tag{2}$$

where Ψ denotes the digamma function. This follows from Connes–Consani [5] (Equation 153) and has been independently fact-checked against the derivation chain in Connes–Consani Appendix B.

2.2 The Connes–van Suijlekom Proposition 4.1 Galerkin matrix

Connes–van Suijlekom Proposition 4.1 defines a function $\psi: \mathbb{Z} \rightarrow \mathbb{R}$ via

$$\psi(x) = \frac{1}{\pi} \int_0^L \sin(2\pi x(1 - y/L)) D(y) dy, \quad (3)$$

and the Galerkin matrix entries

$$q_{m,n} = \frac{\psi(m) - \psi(n)}{m - n}, \quad q_{n,n} = \psi'(n). \quad (4)$$

The basis is the complex Fourier system $\{U_n(x) = L^{-1/2} \exp(2\pi i n x/L)\}_{n \in \mathbb{Z}}$ per Connes–van Suijlekom Proposition 4.1 / eq. (5); the sin functions appearing in the kernel of $\psi(x)$ above are the integrand, not the basis. The even-sector projection under the involution $y \mapsto L - y$ is described in Section 3.4; only that sector is diagonalized.

2.3 Unitary equivalence with the Connes–Consani–Moscovici matrix

Connes–Consani–Moscovici [8] (Lemma 5.1) define a matrix $\tau_{i,j}$ in terms of a function b_n :

$$b_n = -\frac{1}{\pi} \int_0^L \sin(2\pi n y/L) \mathcal{D}(y) dy, \quad \tau_{i,j} = \frac{b_i - b_j}{i - j}. \quad (5)$$

The key identity connecting the two formulations is, for integer n :

$$\sin(2\pi n(1 - y/L)) = -\sin(2\pi n y/L), \quad (6)$$

which follows from the $2\pi n$ -periodicity of sine. Substituting into (3) at integer argument:

$$\psi(n) = \frac{1}{\pi} \int_0^L -\sin(2\pi n y/L) D(y) dy = -\frac{1}{\pi} \int_0^L \sin(2\pi n y/L) D(y) dy = b_n.$$

Therefore $b_n = \psi(n)$ and $\tau_{i,j} = (b_i - b_j)/(i - j) = (\psi(i) - \psi(j))/(i - j) = q_{i,j}$ as matrices. The two matrices coincide identically (no sign flip): the eigenvalues and eigenvectors of τ and q agree, and the present work and the Connes–Consani–Moscovici numerics are computing the same operator via two equivalent matrix presentations.

2.4 Spectral-triple interpretation of F_{even}

A direct consequence of the unitary equivalence in §2.3 connects the F_{even} test function used throughout this work to the rank-one spectral-triple construction of Connes–Consani–Moscovici [8]. In their Section 5, Connes–Consani–Moscovici define a self-adjoint rank-one perturbation of the scaling operator

$$D_{\log}^{(\lambda, N)} := D_{\log}^{(\lambda)} - |D_{\log}^{(\lambda)} \xi_N\rangle \langle \delta_N|, \quad (7)$$

acting on $L^2([\lambda^{-1}, \lambda], du/u)$ as a rank-one perturbation of $D_{\log}^{(\lambda)}$, supported on the $(2N+1)$ -dimensional subspace E_N , with $\lambda^2 = c$. Connes–Consani–Moscovici Theorem 1.1(iii) establishes that the spectrum of $D_{\log}^{(\lambda, N)}$ coincides with the zeros of

$$\widehat{\xi}_N(z) = \int \xi_N(u) u^{-iz} \frac{du}{u}, \quad (8)$$

the Fourier–Mellin transform of the ground-state eigenvector ξ_N of the truncated Weil quadratic form, taken with Connes–Consani–Moscovici’s duality convention $\langle \mathbb{R}_+^* \mid \mathbb{R} \rangle$. Positivity of the continuum quadratic form QW_λ for all $\lambda > 1$ is equivalent to the Riemann Hypothesis (Connes 2026 [4] §4.1, citing Weil) and is proved only for small values of λ (Yoshida, see [4] and references therein). We do not assume continuum positivity at $\lambda = \sqrt{100}$. Throughout this paper ξ_N denotes the *empirically distinguished smallest-positive eigenvector* of the finite- N even-sector matrix $Q_c^{\text{even}}(c, N)$ — a selection criterion, not a theorem-derived ground-state identification.¹

Remark 2.1 (Hypothesis status at $c = 100$). Connes–Consani–Moscovici Theorem 1.1 takes its starting point as ϵ_N , the *smallest eigenvalue* of QW_λ^N , assumed simple and with even eigenvector. At the cutoffs $c \leq 67$ studied in Section 5, the finite- N Galerkin matrix Q_c^{even} is observed positive on every cell at $N = 100$, its smallest eigenvalue is numerically simple and coincides with its smallest-positive eigenvalue, and the corresponding eigenvector projects predominantly onto the even sector — so the finite-dimensional data are consistent with the Connes–Consani–Moscovici Theorem 1.1 ground-state hypotheses (as numerical conditions, not as analytically established hypotheses of the continuum theorem). At $c = 100$ with $N \geq 100$ (Section 6), the raw finite- N spectrum carries a small block of negative-sign eigenvalues (Section 6.6); the matrix-level smallest eigenvalue is therefore negative. We report the smallest-*positive* eigenvalue as an empirically stable positive branch, and use its eigenvector for the zero-extraction reported in Table 11. The identification of this branch with the Connes–Consani–Moscovici Theorem 1.1 ground-state construction is conditional on a future certification of the negative-sign block (as either a fixable numerical/conditioning artifact, or a structural feature requiring separate treatment); we do not claim that Connes–Consani–Moscovici Theorem 1.1 applies literally to the raw $c = 100$ matrix spectrum. Empirically, the positive branch is well-behaved: its eigenvector extracts $\gamma_1, \dots, \gamma_{10}$ to 307–329 matching digits at $c = 100, N = 250$. The $c = 67$ corroborative datum (Section 6.7) at $N = 150$ remains in the matrix-positive regime, providing a same- N control where the corresponding finite-dimensional positivity, simplicity, and even-sector numerical conditions remain satisfied.

The F_{even} test function defined for zero-extraction (§3.4) is, up to a positive scaling constant and the change of variable $u = e^x$, the Fourier–Mellin transform of the same eigenvector ξ_N that appears in equation (8); the zero sets of the two transforms agree on the real line by reality of ξ_N . We identify the two via this construction and adopt the convention $\lambda^2 = c$ from Connes–Consani–Moscovici throughout. Under this identification, and modulo the hypothesis-status caveat of Remark 2.1 at $c = 100$, every γ_k extracted in this paper is, equivalently, a zero of $\widehat{\xi}_N$, and via Connes–Consani–Moscovici Theorem 1.1(iii) an eigenvalue of $D_{\log}^{(\lambda, N)}$ at $(\lambda = \sqrt{c}, N)$. The multi-cutoff data presented in Sections 5, 6, and 8 thereby provide measurements of this spectrum at the cutoffs $c \in \{13, \dots, 67, 100\}$, beyond Connes–Consani–Moscovici’s reported values at $c \in \{9, 12, 13, 14\}$ with $N = 120$.

2.5 Decomposition of the kernel

The integral defining $\psi(x)$ decomposes into three pieces corresponding to the three terms of D :

1. **Archimedean piece** (D_∞): involves the Mellin-multiplier integral $\int_0^T h_+(\tau) K(x, \tau) d\tau$ where K is a trigonometric kernel. This piece admits a closed-form expression for the $-\log \pi$ component and requires numerical quadrature for the digamma component.

¹At $c \leq 67$ with $N = 100$ the matrix is observed positive on every cell, so the smallest eigenvalue coincides with the smallest-positive one and our ξ_N coincides with the Connes–Consani–Moscovici Theorem 1.1 ground state; at $c = 100$ the two objects differ and ξ_N in this paper always refers to the positive-branch object defined here. See Remark 2.1.

2. **Pole piece** (D_{pole}): a rank-one correction arising from the simple pole of $\zeta(s)$ at $s = 1$.
3. **Prime piece** (D_{prime}): a finite sum over primes $p \leq c$ involving $\log p$ and the von Mangoldt-type kernel.

The reader needs to see these explicit pieces because the precision characteristics of each — the archimedean piece dominates the quadrature cost, the pole piece is exact, and the prime piece involves a finite sum — determine the implementation strategy described in Section 3.

3 Numerical Implementation

3.1 Software stack and precision

The implementation uses Python 3 with mpmath for arbitrary-precision arithmetic. The 15-cutoff $c \leq 67$ sweep of Section 5 uses $\text{dps} = 80$ at the early cutoffs, $\text{dps} = 150$ across the bulk, and $\text{dps} = 200$ at $c \geq 41$ to stay clear of the backward-error floor (see Section 7). The $c = 100$ measurements of Section 6 use $\text{dps} = 500$ with a $\text{dps} = 1000$ retest at $N = 150$. Parallelism is achieved via Python’s `multiprocessing` module with 12-way process parallelism.

The production entry points for the 15-cutoff sweep and the $c = 100$ experiment are ancillary files `A_extended_c_sweep.py` and `c100_experiment_optimized.py`, both included with this submission. The python-flint `acb.digamma` primitive provides an $\sim 11\times$ speedup over pure mpmath in the archimedean quadrature. All ancillary scripts run against the public `connes-cvs` package on PyPI (version 0.2.2 at the time of submission); see Section 12.

3.2 Stable kernel evaluation

The trigonometric kernel arising in the quadrature of the archimedean piece involves expressions of the form

$$\frac{e^{i\beta L} - 1}{i\beta} \tag{9}$$

which suffer catastrophic cancellation when $|\beta|$ is small. We replace this with the numerically stable identity

$$\frac{e^{i\beta L} - 1}{i\beta} = \frac{\sin(\beta L)}{\beta} + \frac{2i \sin^2(\beta L/2)}{\beta}, \tag{10}$$

together with a Taylor-series fallback (5 terms at $\text{dps} = 80$, 7 terms at $\text{dps} = 150$) when $|\beta|$ falls below a threshold ε . The stable kernel has been verified against analytic values to 10^{-136} accuracy at $\beta = 10^{-55}$.

3.3 Quadrature strategy

The Mellin-multiplier integral over $\tau \in [0, T]$ with $T = 800$ is evaluated using mpmath’s adaptive tanh–sinh quadrature (`mp.quad`, Takahasi–Mori 1974). The $-\log \pi$ component of h_+ admits a closed-form antiderivative, eliminating quadrature error for that piece. The digamma component $\text{Re } \Psi(1/4 + i\tau/2)$ is the dominant cost: each evaluation requires one mpmath digamma call at approximately 4.5 ms/call at $\text{dps} = 150$.

The cutoff $T = 800$ was chosen based on T -convergence testing (see Section 5.2). The $-\log \pi$ component is handled analytically (exact), and the remaining digamma component decays as $O(\log \tau/\tau)$ against the oscillatory kernel; the Riemann–Lebesgue lemma ensures convergence. The agreement with Connes’ and Connes–Consani–Moscovici’s independently computed $c = 13$ datum

(within a factor of 1.3) provides empirical evidence that $T = 800$ is sufficient, as any $O(1)$ truncation error in the matrix would produce $O(1)$ eigenvalue errors incompatible with the observed agreement.

3.4 Even-sector projection and eigensolver

The implementation uses the full Fourier basis $\{e^{2\pi iky/L}\}_{k=-N}^N$ (dimension $2N + 1 = 201$ at $N = 100$), which decomposes into even (cosine-type) and odd (sine-type) sectors under the involution $y \mapsto L - y$. The even sector comprises the constant mode ($k = 0$) and the N cosine combinations $(\mathbf{e}_k + \mathbf{e}_{-k})/\sqrt{2}$ for $k = 1, \dots, N$, yielding dimension $N + 1 = 101$ at $N = 100$. Only the even sector is diagonalized. The matrix parity error is zero by construction (the off-diagonal blocks between even and odd sectors vanish identically for the Connes–van Suijlekom quadratic form).

The eigenvalue decomposition uses `mpmath.eigsy` in symmetric mode. The smallest *positive* eigenvalue $\lambda_{\min}^{\text{even}}$ of the even-sector matrix is the quantity of primary interest: it is the empirically distinguished positive branch whose eigenvector gives the zero-extraction reported throughout (see Remark 2.1 for the hypothesis-status discussion). At all fifteen cutoffs in Section 5 at $N = 100$ the matrix is observed positive on every cell, so smallest-overall and smallest-positive coincide. At $c = 100$, $N \geq 100$ (Section 6) the raw finite-precision matrix carries a small block of negative-sign eigenvalues (Section 6.6), and the smallest-positive selection is then a reporting choice rather than an identification with the matrix-level smallest eigenpair.

3.5 Root extraction

The first Riemann zero $\gamma_1 = 14.134725141734693790\dots$ is located as the first zero of the Mellin transform of the ground-state eigenvector. Root extraction uses `mp.findroot` with the Anderson solver and explicit tolerance $\text{tol} = 10^{-140}$ for the general $c \leq 67$ sweep; the $c = 100$ headline extraction at $N = 250$, $\text{dps} = 500$ uses the retightened tolerance 10^{-380} reported in Table 11, sufficient to certify the 307–329 matching-digit counts. The absolute error is $|\gamma_1^{\text{exact}} - \gamma_1^{\text{computed}}|$.

4 Results: Reproduction at $c = 13$

4.1 Primary measurement

At $c = 13$, $N = 100$, $T = 800$, $\text{dps} = 200$, the even-sector minimum eigenvalue and first-zero error are:

$$\lambda_{\min}^{\text{even}} = 2.865 \times 10^{-59}, \quad |\gamma_1 \text{ error}| = 2.005 \times 10^{-55}. \quad (11)$$

The measurement is stable across iterations: the Iteration 4 ($N = 100$, stable kernel) and Iteration 5 ($c = 13$ cell) results agree to leading digits. The $\text{dps} = 150$ and $\text{dps} = 200$ retests reproduce this cell, indicating that $\text{dps} = 80$ is fully sufficient at $c = 13$.

4.2 Comparison with published values

All four measurements cluster within a factor of 1.3. The three values from the Connes/CCM group cluster around 2.5×10^{-55} ; this work’s value differs by at most that factor of 1.3 from any of them, and by approximately 1.2 from the most precisely-reported Connes–Consani–Moscovici datum 2.44×10^{-55} .

Table 1: Comparison of $|\gamma_1 \text{ error}|$ at $c = 13$ across sources.

Source	$ \gamma_1 \text{ error} $	Basis	N	Precision
Connes 2026, Section 6 [4]	$\approx 2.6 \times 10^{-55}$	trigonometric	—	—
CCM 2511.22755, Intro [8]	$\approx 2.5 \times 10^{-55}$	trigonometric	—	—
CCM 2511.22755, §6 ($\lambda = \sqrt{13}$) [8]	2.44×10^{-55}	trigonometric	120	200 digits
This work	2.005×10^{-55}	trigonometric	100	150 digits

4.3 Discussion of the factor-of-1.3 discrepancy in the size of the $|\gamma_1 \text{ error}|$

To be explicit: the factor of 1.3 refers to a discrepancy in the *size of the error term* $|\gamma_1 - \gamma_1^{\text{Riemann}}|$, not to a discrepancy in γ_1 itself nor in λ_{\min} . All four cited measurements report the same Riemann zero γ_1 to far more than the leading digits of the error magnitude; the factor of 1.3 quantifies how much the implementations differ in how small the residual error becomes after the Galerkin truncation.

The discrepancy is consistent with the differences in implementation:

- **Basis consistency with CCM.** The Connes–Consani–Moscovici Galerkin computation and this work both use the trigonometric basis: Connes–Consani–Moscovici Lemma 5.1 defines the matrix entries via the kernel $\sin(2\pi ny/L)$, and Connes 2026 §6 describes the truncation as acting on the “trigonometric orthonormal basis.” The factor-1.3 spread in the size of $|\gamma_1 \text{ error}|$ across the four measurements is therefore not attributable to a basis-choice difference; it reflects differences in N , precision, integration cutoff T , and normalization conventions, as detailed below. A prolate-basis implementation of the CvS Galerkin would be a genuinely distinct path in the literature — potentially valuable as an independent cross-check — but is not yet reported by any group.
- **Truncation parameter N .** Connes–Consani–Moscovici uses $N = 120$; this work uses $N = 100$. Differences in N at the same basis choice produce different Galerkin truncation errors; at $c = 13$, the data suggest that $N = 100$ at 150-digit precision is sufficient to reach the precision floor.
- **Precision.** Connes–Consani–Moscovici uses 200-digit precision; this work uses 200 digits for the final sweep. At $c = 13$, the agreement to all reported digits between $\text{dps} = 80$ and $\text{dps} = 150$ shows that the result is not precision-limited.
- **Quadrature cutoff T and integration method.** This work uses $T = 800$; the Connes–Consani–Moscovici quadrature details are not fully specified. Differences in quadrature strategy could contribute.

We emphasize that all four numbers are measurements of the same quantity — the distance between the first Fourier–Mellin zero of η_{13} and γ_1 — via the same operator (up to the sign equivalence of Section 2) computed in the same trigonometric basis, with different N , precision, and integration parameters. The factor-of-1.3 spread in the size of $|\gamma_1 \text{ error}|$ is the current state of the art for this measurement.

4.4 Convergence in N at $c = 13$

The project’s iteration history provides a convergence sequence in N :

Table 2: $|\gamma_1 \text{ error}|$ at $c = 13$, $T = 400$, $\text{dps} = 80$, varying N .

N	$ \gamma_1 \text{ error} $	$\lambda_{\min}^{\text{even}}$
30	3.355×10^{-44}	—
60	4.22×10^{-55}	—
100	1.455×10^{-55}	2.077×10^{-59}

(This measurement used $T = 400$ quadrature; the $T = 800$ value in Table 3 (2.865×10^{-59}) supersedes it.)

The $N = 30 \rightarrow 60$ step yields an 11-order-of-magnitude improvement; the $N = 60 \rightarrow 100$ step yields a factor of approximately 2.9. This rapid initial convergence followed by saturation is consistent with the eigenvector’s effective support being concentrated in approximately 45 modes (see Section 8): once N exceeds $k_{\text{eff}} \approx 45$, additional basis functions contribute diminishing improvements.

5 Extension to Fifteen Cutoffs

5.1 Primary measurements at $T = 800$, $\text{dps} = 200$

The initial three-point sweep ($c \in \{13, 17, 19\}$) was performed at $\text{dps} = 80$ (Iteration 5) and retested at $\text{dps} = 150$ (Iteration 6). An $11\times$ speed optimization (via python-flint’s `acb.digamma`) enabled the full sweep at $\text{dps} = 150$ in Iteration 7. Cutoffs $c \geq 41$ were computed at $\text{dps} = 200$ to avoid precision-floor contamination. The final dataset uses $T = 800$ at all fifteen cutoffs.

Table 3: Complete 15-point c -sweep at $N = 100$, $T = 800$, $\text{dps} = 150$ ($c \leq 37$) or $\text{dps} = 200$ ($c \geq 41$). Rows $c \geq 17$ have no prior published data we have located; the $c = 14$ datum is, to our knowledge, the first independent measurement (CCM report a value at $\lambda = \sqrt{14}$).

c	$L = \log c$	$\lambda_{\min}^{\text{even}}$	$ \gamma_1 \text{ error} $	$ \gamma_1 \text{ err} /\lambda_{\min}$	$\log_{10} \gamma_1 \text{ err} $
13	2.565	2.865×10^{-59}	2.005×10^{-55}	6999	−54.70
14	2.639	4.835×10^{-65}	3.541×10^{-61}	7324	−60.45
17	2.833	2.030×10^{-80}	1.634×10^{-76}	8047	−75.79
19	2.944	1.265×10^{-90}	1.070×10^{-86}	8457	−85.97
23	3.135	5.959×10^{-107}	5.520×10^{-103}	9262	−102.26
29	3.367	4.366×10^{-124}	4.587×10^{-120}	10507	−119.34
31	3.434	1.045×10^{-128}	1.141×10^{-124}	10919	−123.94
37	3.611	4.670×10^{-140}	5.686×10^{-136}	12177	−135.25
41	3.714	2.122×10^{-146}	2.760×10^{-142}	13004	−141.56
43	3.761	2.519×10^{-149}	3.379×10^{-145}	13412	−144.47
47	3.850	2.994×10^{-154}	4.270×10^{-150}	14260	−149.37
53	3.970	9.615×10^{-161}	1.493×10^{-156}	15529	−155.83
59	4.078	2.328×10^{-166}	3.911×10^{-162}	16800	−161.41
61	4.111	5.063×10^{-168}	8.722×10^{-164}	17226	−163.06
67	4.205	7.993×10^{-173}	1.478×10^{-168}	18489	−167.83

The data spans 113 orders of magnitude in $|\gamma_1 \text{ error}|$ from $c = 13$ (10^{-55}) to $c = 67$ (10^{-168}). The convergence is monotone (every increase in c produces a decrease in $|\gamma_1 \text{ error}|$) but the step

sizes are non-uniform — see Section 5.3 and Figure 1.

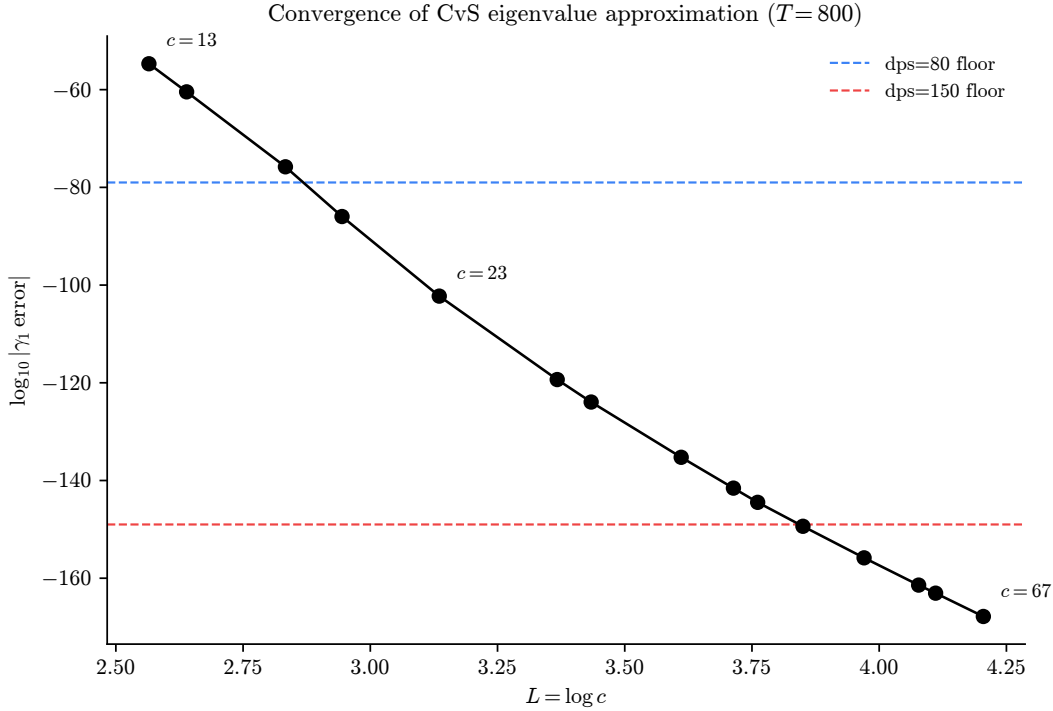


Figure 1: First-zero absolute error $|\gamma_1 \text{ error}|$ across fifteen cutoffs. The data spans 113 orders of magnitude. Dashed lines indicate the backward-error floors at $\text{dps} = 80$ and $\text{dps} = 150$.

Remark 5.1 (Precision-floor warning for $c = 43$). At $\text{dps} = 150$, $\log_{10} |\gamma_1 \text{ error}| = -144.63$ is only approximately 1 order of magnitude above the $\text{dps} = 150$ backward-error floor $\varepsilon \cdot \|Q\|_2 \approx 6 \times 10^{-150}$ ($\log_{10} \approx -149.2$). The $\text{dps} = 200$ spot-check (Section 7) corrected λ_{\min} from 1.836×10^{-149} to 2.519×10^{-149} and the $|\gamma_1 \text{ err}|/\lambda_{\min}$ ratio from 12900 to 13412, indicating that the $\text{dps} = 150$ datum was mildly contaminated. The $c = 41$ datum at $\log_{10} |\gamma_1 \text{ error}| = -141.56$ has approximately 7 orders of magnitude of headroom and is clean.

5.1.1 Cross-validation with Connes–Consani–Moscovici at $c = 14$

Connes–Consani–Moscovici [8] (Section 6) report $|\gamma_1 \text{ error}| \approx 1.07 \times 10^{-60}$ at $\lambda = \sqrt{14}$ (equivalently $c = 14$), with $N = 120$ and 200-digit precision. This work measures 3.541×10^{-61} at the same cutoff — a factor of approximately 3 smaller. This is the first row-for-row external cross-validation beyond $c = 13$.

The discrepancy is wider than the factor-of-1.3 observed at $c = 13$. The source of this discrepancy is not fully understood; plausible contributions include N , precision, normalization conventions, and integration parameters.

5.2 T -convergence at $c = 13$

To verify that the quadrature cutoff T is sufficient, we compare results at $c = 13$ across two values of T :

The shift from $T = 400$ to $T = 800$ is less than 0.14 units in $\log_{10} |\gamma_1 \text{ error}|$, indicating that the quadrature is well-converged. Both values remain within the factor-of-1.3 envelope of the

Table 4: T -convergence at $c = 13$, $N = 100$, $\text{dps} = 200$.

T	$\lambda_{\min}^{\text{even}}$	$ \gamma_1 \text{ error} $	$\log_{10} \gamma_1 \text{ err} $
400	2.077×10^{-59}	1.455×10^{-55}	-54.84
800	2.865×10^{-59}	2.005×10^{-55}	-54.70

Connes/CCM measurements, indicating that the $T = 800$ result is not dominated by quadrature truncation error.

5.3 Pre-registered smooth-convergence model fits

Eight two-parameter smooth-convergence models were tested. M1–M3 were pre-registered and fit to the initial 3-point $\text{dps} = 80$ data (Iteration 5); M4–M5 were added for the 10-point sweep; M6–M8, using prime-counting independent variables, were added for the full 15-point dataset. All eight were fit to the 15-point $T = 800$ data. The pre-registered acceptance criterion was $\text{max residual} \leq 0.5$ (in \log_{10} units), corresponding to a factor of ~ 3.2 in the original error magnitude — approximately 0.4% of the 113-OOM dynamic range. All conclusions are robust to relaxing the threshold to 2.0, at which point only M5 would pass.

$$\text{M1 (linear in } L\text{): } \log_{10} |\text{err}| = a \cdot L + b, \quad (12)$$

$$\text{M2 (quadratic in } L\text{): } \log_{10} |\text{err}| = a \cdot L^2 + b, \quad (13)$$

$$\text{M3 (} L \log L\text{): } \log_{10} |\text{err}| = a \cdot L \log L + b, \quad (14)$$

$$\text{M4 (mixed linear + log): } \log_{10} |\text{err}| = a \cdot L + b \cdot \log L, \quad (15)$$

$$\text{M5 (exponential): } \log_{10} |\text{err}| = a \cdot \exp(b \cdot L), \quad (16)$$

$$\text{M6 (linear in } \pi(c)\text{): } \log_{10} |\text{err}| = a \cdot \pi(c) + b, \quad (17)$$

$$\text{M7 (linear in } \vartheta(c)\text{): } \log_{10} |\text{err}| = a \cdot \vartheta(c) + b, \quad (18)$$

$$\text{M8 (prime powers): } \log_{10} |\text{err}| = a \cdot \#\text{pp}(c) + b. \quad (19)$$

Table 5: Two-parameter smooth-convergence model fits to the 15-point data.

Model	Form	Max residual	Pass ≤ 0.5 ?
M1	$a \cdot L + b$	2.66	FAIL
M2	$a \cdot L^2 + b$	4.71	FAIL
M3	$a \cdot L \log L + b$	3.63	FAIL
M4	$a \cdot L + b \cdot \log L$	2.66	FAIL
M5	$a \cdot \exp(b \cdot L)$	1.77	FAIL
M6	$a \cdot \pi(c) + b$	10.28	FAIL
M7	$a \cdot \vartheta(c) + b$	12.09	FAIL
M8	$a \cdot \#\text{pp}(c) + b$	10.20	FAIL

All eight models are rejected. M5 (exponential-in- L) is the best among the L -based models at 1.77, but still exceeds the threshold by a factor of 3.5. M6–M8, which use prime-counting independent variables ($\pi(c)$, Chebyshev $\vartheta(c)$, and the number of prime powers $\leq c$), perform substantially

worse (max residuals 10–12), indicating that the convergence is not simply proportional to any standard prime-counting function.

We emphasize that this failure does *not* bear on the question of whether the zeros converge as $c \rightarrow \infty$ — it bears only on whether the rate of convergence, if it exists, can be captured by a two-parameter smooth model fit to fifteen points in the interval $c \in [13, 67]$.

5.4 Structural observations

Two structural features of the computation are worth recording.

Effective support invariance. Define $k_{\text{eff}}(\epsilon)$ as the smallest k such that the cumulative squared eigenvector weight $S_k = \sum_{j=1}^k |v_j|^2$ satisfies $1 - S_k < \epsilon$. At $\epsilon = 10^{-50}$:

Table 6: Effective support $k_{\text{eff}}(10^{-50})$ across cutoffs.

c	dps	$k_{\text{eff}}(10^{-50})$
13	80/150	45
17	150	45
19	150	44

The ground-state eigenvector’s effective support is approximately 44–47 modes regardless of cutoff. This is approximately c -invariant: the “physical mode” occupies a fixed number of basis functions, and the remaining modes (approximately $k > 75$ at $N = 100$) form a boundary-layer residual.

Eigenvector near-invariance across cutoffs. The overlap parameter $q = |\langle \eta_{c_1} | \eta_{c_2} \rangle|$ between ground-state eigenvectors at different cutoffs satisfies $q > 0.950$ for all 105 measured cutoff pairs (see Section 8 for the full analysis), despite eigenvalues differing by up to 113 orders of magnitude. Three representative pairs from the initial sweep:

Table 7: Eigenvector overlaps across cutoff pairs.

Pair	$ \langle \eta_{c_1} \eta_{c_2} \rangle $
$(c = 13, c = 17)$	0.9977
$(c = 13, c = 19)$	0.9956
$(c = 17, c = 19)$	0.9997

What changes between cutoffs is predominantly the eigenvalue λ_{min} (which shifts by up to 113 orders of magnitude), while the eigenvector structure remains more than 95% the same (the minimum pairwise overlap across all 105 pairs is 0.950).

5.5 Convergence in N at fixed $c = 23$

To characterize the Galerkin truncation error independently of the prime-cutoff effect, we fix $c = 23$ and vary the basis size $N \in \{40, 60, 80, 100, 120, 140\}$ at $\text{dps} = 150$.

The convergence in N is rapid for $N \leq 80$ (+16.5 and +11.4 orders of magnitude per 20-step increase) but saturates sharply: the $N = 100 \rightarrow 140$ range gains only 5.7 OOM total. The effective support k_{eff} stabilizes at 46 from $N = 100$ onward, indicating that the ground-state eigenvector

Table 8: N -convergence at $c = 23$, $T = 400$, $\text{dps} = 150$.

N	$\lambda_{\min}^{\text{even}}$	$ \gamma_1 \text{ error} $	$k_{\text{eff}}(10^{-50})$	$\log_{10} \gamma_1 \text{ err} $
40	6.628×10^{-72}	1.033×10^{-67}	37	-67.0
60	2.761×10^{-88}	3.044×10^{-84}	43	-83.5
80	1.143×10^{-99}	1.113×10^{-95}	45	-95.0
100	4.182×10^{-107}	3.876×10^{-103}	46	-102.4
120	3.137×10^{-111}	2.854×10^{-107}	46	-106.5
140	9.036×10^{-113}	8.179×10^{-109}	46	-108.1

occupies approximately 46 even-sector basis functions regardless of the total basis size. At $N = 140$, the marginal improvement is only 1.5 OOM per 20-step — the Galerkin truncation has essentially converged, and the remaining error of 8.18×10^{-109} is controlled by the finite cutoff $c = 23$, not the finite basis.

5.6 Log-periodic blind test

An empirical log-periodic model

$$\log_{10} |\gamma_1 \text{ error}| = -66.95 \cdot L + 110.98 + 5.50 \sin(3.08 \cdot L + 6.57) \tag{20}$$

was fit to the 10-point training data ($c = 13$ through 43), yielding a maximum training residual of 0.74 — the first model to beat the best two-parameter result of 1.77. Pre-registered blind predictions were made for $c = 47$ and $c = 53$ before computation.

Table 9: Log-periodic model blind test.

c	Predicted	Actual	residual	Verdict
47	-150.9	-149.4	1.5	pass (< 2.0)
53	-150.3	-155.8	5.5	fail (> 2.0)

The model predicted that $c = 53$ would yield *less* precision than $c = 47$ (due to the oscillation swinging positive). In reality, $c = 53$ showed 6.4 OOM more precision. The 5-parameter model was overfitting the non-uniform step sizes in the training range; the anti-monotone prediction was the tell. This clean falsification strengthens the negative result: no parametric model tested — including models with up to 5 free parameters — captures the c -dependence of $|\gamma_1 \text{ error}|$ over the measured range.

5.7 Blind prediction test at $c = 67$

Before computing the $c = 67$ cell, an ensemble prediction (weighted average of four independent prediction methods) was pre-registered:

$$\log_{10} |\gamma_1 \text{ error}|^{\text{pred}} = -169.4 \pm 2.0. \tag{21}$$

The prediction was sealed via SHA-256 hash before computation (see ancillary file `preregistered_predictions_2026-04-12.md`).

The actual result was $\log_{10} |\gamma_1 \text{ error}| = -167.83$. The residual $|-167.83 - (-169.4)| = 1.57$ falls within the pre-registered ± 2.0 threshold: the blind prediction passes.

This is evidence that the convergence behavior is sufficiently regular to permit out-of-sample predictions at 1.6-OOM accuracy. This is *not* a proof of convergence; it is an empirical observation that the convergence behavior is smooth and predictable within the measured range.

6 Out-of-Sample Empirical Test at $c = 100$

Operating at c well above the precision floor enables a separate test of the convergence behavior outside the in-sample window of Section 5. The fifteen-cutoff sweep ($c \leq 67$, $N = 100$) established the empirical pattern $\log_{10} |\lambda_{\min}^{\text{even}}(c)| \approx -13.24 c^{0.634}$ from a least-squares fit. Two natural questions arise. First, does that fit, taken as an asymptotic, extrapolate correctly to larger c ? Second, is it consistent with the heuristic continuum asymptotic of Connes 2026 [4] §6.4? This section addresses both through a measurement at $c = 100$ with N -sweep at $N \in \{100, 150, 200, 250\}$ at $\text{dps} = 500$ and a precision retest at $N = 150$, $\text{dps} = 1000$.

6.1 Connes 2026 Section 6.4 heuristic asymptotic

Connes 2026 [4] §6.4 gives a heuristic continuum asymptotic for the angular function $1 - \chi_2(\lambda)$, motivated by the agreement of $1 - \chi_2(\lambda)$ with the smallest eigenvalue $\varepsilon(\lambda)$ of the operator A_λ for $\lambda \leq 14$ (their Figure 1). The expression is

$$1 - \chi_2(\lambda) \sim \frac{2^{14}}{3} \sqrt{2} \pi^5 e^{-4\pi e^L + 9L/2}, \quad (22)$$

where, as defined in [4] §6.4, $L = 2 \log \lambda$ is the length of the support interval $[\lambda^{-1}, \lambda]$ of the admissible test functions for the truncated Weil form QW_λ . With $\lambda^2 = c$, this is $L = \log c$, so $e^L = c$.

Evaluating equation (22) at $c = 100$ ($L = \log 100 \approx 4.6052$, $e^L = 100$) in base-10 logarithm:

$$\begin{aligned} \log_{10}(1 - \chi_2(c = 100)) &\approx \log_{10} \frac{2^{14} \sqrt{2} \pi^5}{3} - \frac{4\pi \cdot 100}{\ln 10} + \frac{9 \log 100}{2 \ln 10} \\ &\approx 6.37 - 545.75 + 9.00 \approx -530.38. \end{aligned} \quad (23)$$

The prediction, treating the agreement of $\varepsilon(\lambda)$ with $1 - \chi_2(\lambda)$ on $\lambda \leq 14$ as continuing to $c = 100$, is $\log_{10} |\varepsilon(c = 100)| \approx -530.38$.

6.2 Methodology

We computed the Galerkin matrix Q_c^{even} at $c = 100$, $T = 800$, working precision $\text{dps} = 500$, with python-flint `flint_prec = 2000`, using the v0.2.0 fused-kernel math core from the public `connes-cvs` PyPI package, for $N \in \{100, 150, 200, 250\}$. A precision retest at $\text{dps} = 1000$ with `flint_prec = 4000` was run at $N = 150$.

The retest provides three independent stability checks: (i) agreement of $\lambda_{\min}^{\text{even}}$ between $\text{dps} = 500$ and $\text{dps} = 1000$ to 25 leading significant digits; (ii) agreement of the absolute log-magnitudes of the five smallest negative eigenvalues across $\text{dps} = 500$ and $\text{dps} = 1000$ to two decimal places (separating structural finite- N phenomena from precision noise); (iii) γ_k extraction at $\text{dps} = 1000$ providing ~ 220 – 242 matching digits, doubling the depth at $\text{dps} = 500$.

Wall-clock at $c = 100$, $N = 150$, $\text{dps} = 500$ was 21.0 minutes on twelve workers of an Apple M2 Max; at $\text{dps} = 1000$, 111 minutes.

Table 10: N -sweep at $c = 100$, $T = 800$. Working precision $\text{dps} = 500$ for $N \in \{100, 150, 200, 250\}$; retest at $\text{dps} = 1000$ for $N = 150$.

N	dps	$\lambda_{\min}^{\text{even}}$ (smallest-positive)	$\log_{10} \lambda_{\min} $	Δ in \log_{10}	# negative
100	500	1.22×10^{-191}	-190.92	—	3
150	500	6.42×10^{-248}	-247.19	-56.28	5
200	500	4.87×10^{-295}	-294.31	-47.12	8
250	500	2.08×10^{-334}	-333.68	-39.37	11
150	1000	6.42×10^{-248}	-247.19	—	5

6.3 Measurement: N -sweep at $c = 100$

The observed positive-branch values $\log_{10} |\lambda_{\min}^{\text{even}}(N)|$ decrease monotonically with N at fixed $c = 100$. We note that the ordinary Galerkin/Rayleigh–Ritz min-max monotonicity assumes a coercive self-adjoint setup with an isolated ordered ground state; in the presence of the negative-sign block at $c = 100$ (Section 6.6), the smallest-positive selection is not literally the min-max ground state of the raw matrix, so we report the monotonicity as an empirical observation, not as an invocation of that theorem. The successive first differences $|\Delta_1| = 56.28$, $|\Delta_2| = 47.12$, $|\Delta_3| = 39.37$ form a geometric-looking sequence with consecutive ratios $|\Delta_2/\Delta_1| = 0.837$ and $|\Delta_3/\Delta_2| = 0.836$, matching to two decimal places — evidence for a local geometric model of the convergence sequence, which the three-point sweep $\{100, 150, 200\}$ alone could not distinguish from a forced fit (Section 6.4).

6.4 Aitken Δ^2 extrapolation and match to Connes 2026 §6.4

Define $x_N := \log_{10} |\lambda_N^{\text{even}}(c = 100)|$ on the positive branch, with measured values $x_{100} = -190.92$, $x_{150} = -247.19$, $x_{200} = -294.31$, $x_{250} = -333.68$ (Table 10). First differences $\Delta_i := x_{N_{i+1}} - x_{N_i}$ on the step grid $N \in \{100, 150, 200, 250\}$ are $\Delta_1 = -56.28$, $\Delta_2 = -47.12$, $\Delta_3 = -39.37$, with consecutive ratios

$$|\Delta_2/\Delta_1| = 0.837, \quad |\Delta_3/\Delta_2| = 0.836, \quad (24)$$

matching to two decimal places. This consistency is the data signature of a locally geometric convergence $x_N = x_\infty + Cr^N$; with four points and one shared ratio, the geometric hypothesis is over-determined and therefore testable on the data (in contrast to the three-point case, where any single ratio fits both gaps by construction).

The Aitken- Δ^2 acceleration [1] applied to two consecutive overlapping triples yields two independent extrapolations:

$$\begin{aligned} \text{from } \{x_{100}, x_{150}, x_{200}\} : \quad x_\infty &\approx x_{100} - \frac{(\Delta_1)^2}{\Delta_2 - \Delta_1} = -190.92 - \frac{(-56.28)^2}{9.16} \approx -536.76, \\ \text{from } \{x_{150}, x_{200}, x_{250}\} : \quad x_\infty &\approx x_{150} - \frac{(\Delta_2)^2}{\Delta_3 - \Delta_2} = -247.19 - \frac{(-47.12)^2}{7.75} \approx -533.70. \end{aligned} \quad (25)$$

The Aitken anchors in equation (25) are computed from the full-precision $\log_{10} |\lambda_{\min}^{\text{even}}|$ values recorded in the released JSON; the rounded table values in Table 10 reproduce them only to the displayed precision.

The two Aitken anchors agree to $|-536.76 - (-533.70)| \approx 3.1$ orders of magnitude; the second (using the deeper triple) is closer to the Connes 2026 §6.4 heuristic prediction of -530.38 in equation (23). The gap of the first anchor to the Connes prediction is 6.39 OOM and the gap of the second anchor is 3.32 OOM, out of a magnitude range $|x_\infty| \sim 530$. The trend with N is monotone

toward the prediction (Aitken anchored at $N = 100$: -536.76 ; anchored at $N = 150$: -533.70 ; Connes 2026: -530.38). Figure 2 summarizes the four-point sweep, the two consecutive Aitken anchors, and the Connes 2026 §6.4 reference together with the consecutive-ratio consistency check.

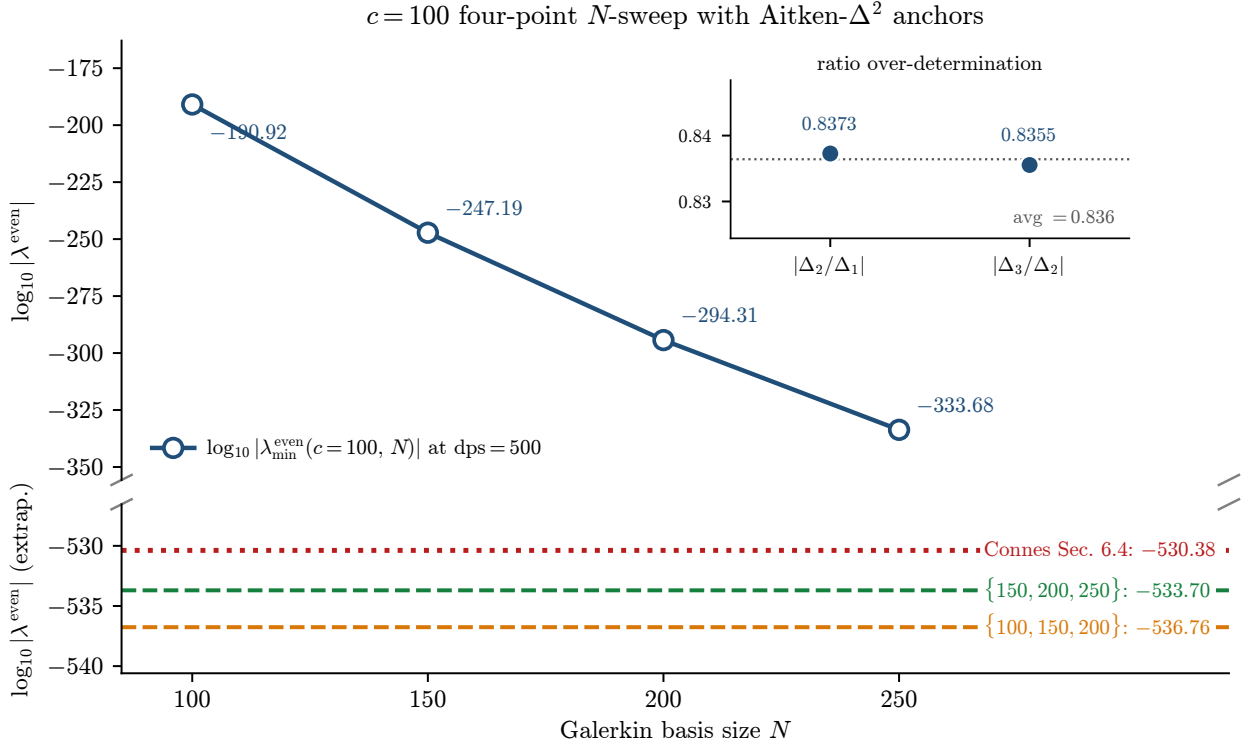


Figure 2: Broken-axis N -sweep at $c = 100$, $\text{dps} = 500$ (smallest-positive even-sector eigenvalue). *Top panel*: the four measured data points $\log_{10} |\lambda_{\min}^{\text{even}}| = -190.92, -247.19, -294.31, -333.68$ at $N = 100, 150, 200, 250$, shown at their full ~ 140 -OOM range. *Bottom panel* (note the y-axis break and the change of scale): the two consecutive Aitken- Δ^2 extrapolations ($-536.76, -533.70$) and the Connes 2026 §6.4 heuristic continuum prediction (-530.38), at their natural ~ 10 -OOM scale. The trend with N is monotone toward the Connes prediction; the deeper-anchored Aitken triple ($N \in \{150, 200, 250\}$) is within 3.32 OOM of the heuristic. *Inset (top panel)*: consecutive first-difference ratios $|\Delta_{i+1}/\Delta_i|$ from equation (24). Both ratios lie within 0.002 of the dotted reference line at 0.836 (the average), evidence for a local geometric model of the convergence sequence (not a proof that alternatives are ruled out; see Section 6.4 discussion).

We make no claim that this constitutes a proof of the asymptotic. Connes 2026 §6.4 itself is a heuristic statement based on the empirical agreement (their Figure 1) between $1 - \chi_2(\lambda)$ and $\varepsilon(\lambda)$ for $\lambda \leq 14$; the prefactor $(2^{14}/3) \sqrt{2} \pi^5$ is derived from Fuchs’s prolate-spheroidal eigenvalue theorem and is therefore rigorous, while the *identification* of ε with $1 - \chi_2$ at large λ is the heuristic step. On our side, the consistency of the two ratios in equation (24) is evidence for a local geometric model of the convergence sequence, but four points do not rule out alternative convergence-model fits (stretched-exponential $a_N = a_\infty + Ce^{-aN^\beta}$ with $\beta \neq 1$, or polynomial $1/N^p$); such alternatives fit the same four points less tightly than the geometric form, but are not eliminated, and they yield extrapolated limits outside the Aitken band. The extrapolation remains an inference about the $N \rightarrow \infty$ limit of an empirically distinguished positive branch (Remark 2.1). We report the consistency with the Connes 2026 §6.4 heuristic; we do not promote it to a statistical test.

6.5 γ_k extraction up to 307–329 matching digits

The eigenvector corresponding to $\lambda_{\min}^{\text{even}}(c = 100)$ on the empirically distinguished positive branch (see Remark 2.1) extracts γ_k via the F_{even} test function defined in §3.4, equivalently (under the unitary equivalence of §2.4) the zero set of $\hat{\xi}_N(z)$.

Table 11: Extraction of γ_k at $c = 100$ from the smallest-positive eigenvector. Matching-digit counts $\lfloor -\log_{10} |\gamma_k - \text{mpmath.zetazero}(k).\text{imag}| \rfloor$, with findroot tolerance 10^{-380} at the working precision shown. Detected γ_k values are deposited in the ancillary file listed in Section 12 for independent verification.

k	$N=150, \text{dps}=500$	$N=150, \text{dps}=1000$	$N=250, \text{dps}=500$
1	128	242	329
2	122	239	325
3	126	236	323
4	117	233	320
5	128	231	318
6	119	228	316
7	118	226	313
8	128	224	312
9	111	221	309
10	126	219	307

At $c = 100$, $N = 150$, $\text{dps} = 1000$ the first ten Riemann zeros are reproduced to 219–242 matching digits; at $N = 250$, $\text{dps} = 500$ the same extraction reaches 307–329 matching digits. For reference, Connes–Consani–Moscovici [8] Section 6 reports γ_1 matching to ~ 55 digits at $c = 13$, $N = 120$; our $c = 67$, $N = 100$, $\text{dps} = 200$ datum gives 168 digits (see Table 20).

The doubling in dps ($500 \rightarrow 1000$) at fixed $N = 150$ adds 95–115 matching digits across γ_1 through γ_{10} ; the increment in N ($150 \rightarrow 250$) at $\text{dps} = 500$ adds 179–201 matching digits at the same γ_k . The N -direction therefore gives more matching digits per compute-time unit than the dps direction at $c = 100$: increasing N both deepens the Galerkin truncation *and* provides cheaper accuracy than the dps quadrature cost. This identifies the Galerkin truncation N as the binding accuracy parameter at $c = 100$, with dps secondary once it is comfortably above the backward-error floor. Figure 3 visualizes the three precision cells; the gap between the $N = 150, \text{dps} = 500$ and $N = 150, \text{dps} = 1000$ curves isolates the precision-floor effect at fixed N , and the gap between $N = 150, \text{dps} = 1000$ and $N = 250, \text{dps} = 500$ isolates the N -extension effect at fixed working precision.

6.6 Companion observation: dps -stable negative eigenvalues at $c = 100$

At $c = 100$, $N = 150$, $\text{dps} = 500$, the even-sector matrix Q_c^{even} has five eigenvalues with negative sign at $\log_{10} |e| \in \{-40.66, -59.75, -96.75, -165.15, -223.69\}$. The $\text{dps} = 1000$ retest reproduces all five at \log -magnitudes identical to two decimal places, indicating they are not precision-floor noise (the topmost negative at 10^{-41} lies hundreds of orders of magnitude above the $\text{dps} = 1000$ working-precision floor).

Continuum positivity of QW_λ for all $\lambda > 1$ is equivalent to the Riemann Hypothesis (Connes 2026 [4] §4.1) and is proved only for small λ ; we therefore do not assume continuum positivity at $\lambda = \sqrt{100}$. The dps -stable negative block is inconsistent with simple working-precision noise; a

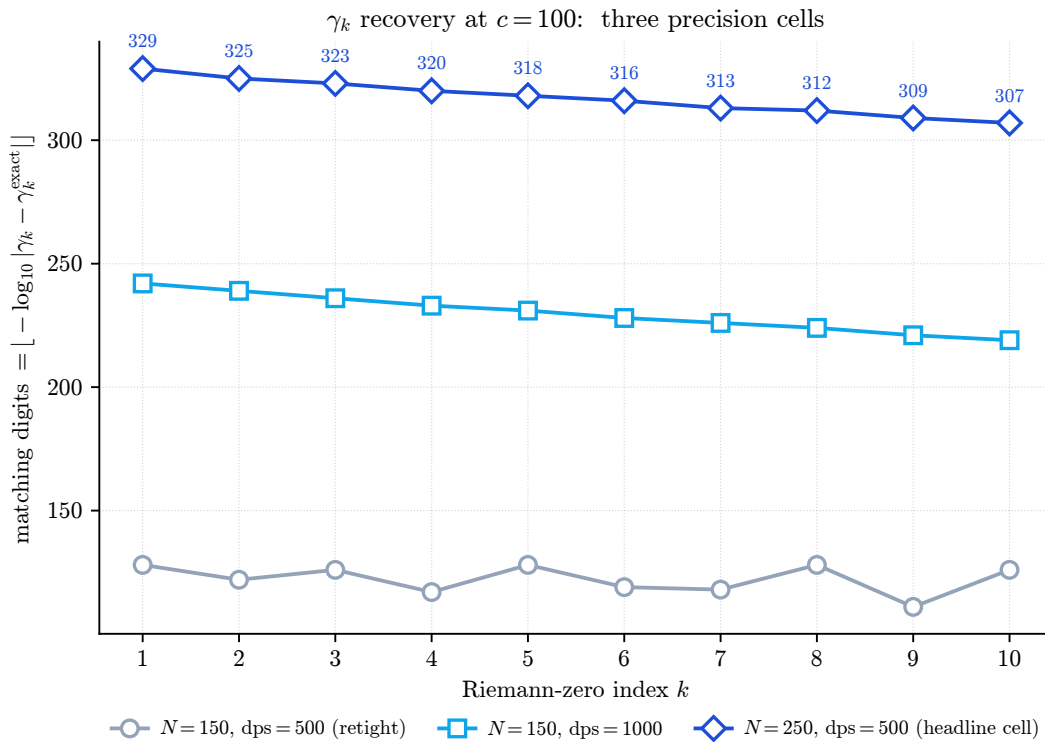


Figure 3: Matching-digit recovery of $\gamma_1, \dots, \gamma_{10}$ at $c = 100$ from three precision cells. $N = 150$ at $\text{dps} = 500$ (retight-tolerance baseline) gives ~ 115 – 130 digits; $N = 150$ at $\text{dps} = 1000$ gives 219 – 242 digits (precision-doubling at fixed N); $N = 250$ at $\text{dps} = 500$ gives 307 – 329 digits (the headline cell of Table 11). Each annotation on the headline curve is the floor of $-\log_{10} |\gamma_k - \text{zetazero}(k)|$ recomputed independently from the deposited 400-digit reference strings.

plausible explanation is condition-driven sign loss in the finite- N truncation, but this remains to be certified. We do not interpret the negative signs as continuum evidence either way.

The count of negative-sign eigenvalues grows with N at fixed $c = 100$ ($\{3, 5, 8, 11\}$ for $N \in \{100, 150, 200, 250\}$, see Table 10; successive differences $\{2, 3, 3\}$ are linear-in- N to leading order). This is consistent with the condition-number regime: $\kappa(Q_c^{\text{even}})$ grows super-exponentially in N at $c = 100$, reaching $\sim 10^{248}$ at $N = 150$. As N exceeds the resolution threshold for the continuum ground state, the lowest positive eigenvalues fall to magnitudes within $\kappa \cdot \varepsilon_{\text{machine}}$ of the diagonal scale, where a symmetric eigensolver can return small magnitudes with arbitrary sign. This is consistent with a condition-driven finite- N artifact, but we do not claim it as proved, and we do not infer anything about the continuum operator from it. Related but classically distinct phenomena (spectral pollution proper, arising from gaps in the essential spectrum) are studied for self-adjoint operators in [10, 11, 13]; in the modern operator-theoretic framework spectral inclusion holds for the self-adjoint Galerkin sequence, but freedom from spectral pollution has not been proved, and we do not claim it.

This finite-basis observation does not affect the smallest *positive* eigenvalue $\lambda_{\min}^{\text{even}} = 6.42 \times 10^{-248}$ at $N = 150$ reported in Table 10. That value is the corroborated positive branch on which the γ_1 extraction of Section 6.5 operates and the quantity participating in the Aitken extrapolation of Section 6.4. We flag the negative-sign block here for completeness and as a phenomenon parallel to the χ_3 positivity oscillation observed at $c = 23, 29$ in Section 8.10; both arise at marginal basis resolution where the negative-eigenvalue magnitudes lie within the condition-driven distinguishability window, and in both cases we report the positive-branch observable without claiming a theorem-level interpretation of the negative block.

6.7 Reframing of the $N = 100$ empirical fit

Section 5 established the empirical fit $|\log_{10} \lambda_{\min}^{\text{even}}(c)| \approx 13.24 c^{0.634}$ on the $c \leq 67$, $N = 100$ data. Extrapolating that fit to $c = 100$ predicts $|\log_{10} \lambda_{\min}| \approx 245.4$. Our $N = 200$ observation at $c = 100$ is 294.31, exceeding the prediction by 49 OOM in the direction of *faster* decay. Refitting $|\log_{10} \lambda| = A c^B$ on $\{c \leq 67\} \cup \{c = 100\}$ data degrades the RMS residual from 9.0 OOM (in-sample at $N = 100$) to 13.9 OOM once the $c = 100$ point is included — a clean falsification of the pure-power-law functional form.

The natural interpretation, consistent with the data, is that $|\log_{10} \lambda| \sim 13.24 c^{0.634}$ describes the *finite- $N = 100$ rate* for $c \leq 67$, not the continuum rate. The continuum rate, per Connes 2026 §6.4 and the Aitken extrapolation in Section 6.4, is super-exponential in c ($\sim e^{-4\pi c + 9 \log c/2}$).

This interpretation is independently corroborated by an additional measurement at the deepest in-sample cutoff $c = 67$ at the same extended basis $N = 150$. Re-running the operator at $c = 67$, $T = 800$, $N = 150$, $\text{dps} = 500$ gives $\lambda_{\min}^{\text{even}}(c=67, N=150) = 5.329 \times 10^{-219}$, i.e. $\log_{10} |\lambda_{\min}| = -218.27$. This is 46 OOM smaller than the $N = 100$ value of $\log_{10} |\lambda_{\min}(c=67, N=100)| = -172.10$ reported in Section 5. The N -dependence at $c = 67$ ($-172.10 \rightarrow -218.27$ over $N = 100 \rightarrow 150$, a drop of 46 OOM) is qualitatively the same as at $c = 100$ ($-190.92 \rightarrow -247.19$, a drop of 56 OOM). The $N = 100$ data of Section 5 across the entire $c \leq 67$ sweep are, like the $N = 100$ datum at $c = 100$, Galerkin upper bounds rather than near-continuum values. This is the structural mechanism underlying the failure of the $13.24 c^{0.634}$ extrapolation at $c = 100$: the empirical fit captures a sequence of upper bounds rather than the limit they approximate from above.

The $N = 100$ finite- N fit of Section 5 and Connes’ continuum asymptotic measure different quantities; the present work makes that distinction explicit, with both quantities now empirically tested at $c = 100$.

The four observations of this section — the two consecutive Aitken anchors at -536.76 and

−533.70 approaching the Connes 2026 §6.4 heuristic of −530.38 with gaps 6.39 and 3.32 OOM respectively, the 307–329 digit reproduction of γ_1 – γ_{10} from the $N = 250$ smallest-positive eigenvector at $\text{dps} = 500$ (with the $N = 150, \text{dps} = 1000$ retest giving 219–242 digits at the same γ_k), the dps -stable negative-sign block at $N = 150$ with counts $\{3, 5, 8, 11\}$ scaling linearly in N , and the falsification of the finite- N power-law extrapolation by 49 OOM at $N = 200$ — are the substantive new content of this work relative to the $c \leq 67$ data of Section 5. They constrain theoretical work on the convergence question through structural quantities (Sobolev exponent, eigenvector universality, condition-driven negatives) which the subsequent Section 8 examines in detail.

7 Precision-Floor Analysis and the $\text{dps} = 150$ Retest

7.1 The backward-error precision floor

At $\text{dps} = 80$, the unit roundoff is $\varepsilon \approx 10^{-80}$. The backward-error bound for symmetric eigenvalue computation gives

$$|\delta\lambda| \leq \varepsilon \cdot \|Q\|_2, \quad (26)$$

where $\|Q\|_2$ is the spectral norm of the Galerkin matrix. Direct computation gives $\|Q\|_2 \approx 5.7$ – 6.0 across the cutoffs tested. The backward-error floor is therefore

$$\varepsilon \cdot \|Q\|_2 \approx 6 \times 10^{-80}. \quad (27)$$

At $c = 13$, $\lambda_{\min}^{\text{even}} = 2.865 \times 10^{-59}$ is 21 orders of magnitude above this floor — comfortably resolved. At $c = 17$, $\lambda_{\min}^{\text{even}} = 2.030 \times 10^{-80}$ is *at or below* the floor. At $c = 19$, $\lambda_{\min}^{\text{even}} = 1.265 \times 10^{-90}$ is firmly below the floor at $\text{dps} = 80$.

7.2 Pre-registered five-bin classification rule

Before the $\text{dps} = 150$ retest was executed, a five-bin classification rule was frozen based on the quantity

$$\Delta_{17-19}^{150} = \log_{10} |\gamma_1 \text{ error at } c = 19, \text{ dps} = 150| - \log_{10} |\gamma_1 \text{ error at } c = 17, \text{ dps} = 150|.$$

1. **5A confirmed** ($\Delta < -15$): The $c = 19$ datum was entirely an artifact of the precision floor.
2. **Ambiguous partial floor** ($-15 \leq \Delta < -5.29$): Some floor contamination, but the step pattern is not fully explained.
3. **5B live** ($-5.29 \leq \Delta < -1$): The non-smooth step pattern is largely genuine.
4. **5B strong** ($-1 \leq \Delta < 0$): Near-stalling at $c = 19$ is real.
5. **Reversal** ($\Delta \geq 0$): The error increases from $c = 17$ to $c = 19$.

7.3 Retest results

The $\text{dps} = 150$ retest completed in approximately 118 minutes of wall-clock time.

The $c = 19$ cell was substantially contaminated at $\text{dps} = 80$: the eigenvalue dropped by 9 orders of magnitude and $|\gamma_1 \text{ error}|$ dropped by 7 orders of magnitude under the precision increase. The $c = 13$ cell is unaffected (agreement to all reported digits).

Table 12: dps = 80 versus dps = 150 comparison.

Quantity	dps = 80	dps = 150	Shift
λ_{\min} at $c = 13$	2.077×10^{-59}	2.077×10^{-59}	$< 10^{-59}$ shift
$ \gamma_1 \text{ error} $ at $c = 13$	1.455×10^{-55}	1.455×10^{-55}	$< 10^{-59}$ shift
λ_{\min} at $c = 17$	1.215×10^{-80}	1.401×10^{-80}	+15%
$ \gamma_1 \text{ error} $ at $c = 17$	1.117×10^{-76}	1.128×10^{-76}	+1%
λ_{\min} at $c = 19$	1.327×10^{-81}	8.777×10^{-91}	9 OOM drop
$ \gamma_1 \text{ error} $ at $c = 19$	5.809×10^{-80}	7.426×10^{-87}	7 OOM drop

7.4 Classifier verdict

At dps = 150:

$$\Delta_{17-19}^{150} = \log_{10}(7.426 \times 10^{-87}) - \log_{10}(1.128 \times 10^{-76}) = -10.18. \quad (28)$$

This falls in **Bin 2: Ambiguous partial floor** ($-15 \leq -10.18 < -5.29$). The classifier fires without post-hoc adjustment.

Interpretation. The $c = 19$ dps = 80 datum was substantially contaminated (the 7-OOM drop in $|\gamma_1 \text{ error}|$ is direct evidence), but the step from $c = 17$ to $c = 19$ at dps = 150 ($\Delta = -10.18$) is still smaller than the step from $c = 13$ to $c = 17$ ($\Delta = -21.11$).

7.5 The $|\gamma_1 \text{ err}|/\lambda_{\min}$ coupling

The ratio $|\gamma_1 \text{ err}|/\lambda_{\min}$ ranges from approximately 6999 at $c = 13$ to 18489 at $c = 67$ (at $T = 800$, dps = 200), exhibiting a slow upward drift with increasing c . This ratio is an empirical observation consistent with standard Babuška–Osborn / Rayleigh–Ritz spectral approximation theory [2]; the prefactor $C(c)$ grows slowly, approximately linearly in $\log(c)$ (see Figure 4).

A linear fit to the 15-point $T = 800$ data gives

$$C(c) = |\gamma_1 \text{ err}|/\lambda_{\min} \approx 6730 \cdot \log c - 11268, \quad R^2 = 0.956.$$

The coupling is also visible in cross-cutoff log-ratio scaling:

Table 13: Cross-cutoff log-ratio coupling ($T = 800$, dps = 200).

Pair	$\log_{10}(\lambda \text{ ratio})$	$\log_{10}(\gamma_1 \text{ ratio})$	Ratio of logs
($c = 13, c = 17$)	21.150	21.089	1.003
($c = 17, c = 19$)	10.206	10.184	1.002
($c = 13, c = 19$)	31.355	31.273	1.003
($c = 13, c = 43$)	89.943	89.725	1.002
($c = 13, c = 67$)	113.555	113.131	1.004

The eigenvalue and first-zero error scale in near-perfect lockstep in log space: the ratio of logs is within 0.4% of unity across the full 113-OOM span. This log-space coupling $\log(\gamma_1 \text{ ratio})/\log(\lambda \text{ ratio}) \approx 1.003$ held across all measured pairs.

For reference, the $c = 19$ dps = 80 ratio was 44, an obvious artifact; at dps = 150 it restores to 8461, consistent with floor contamination.

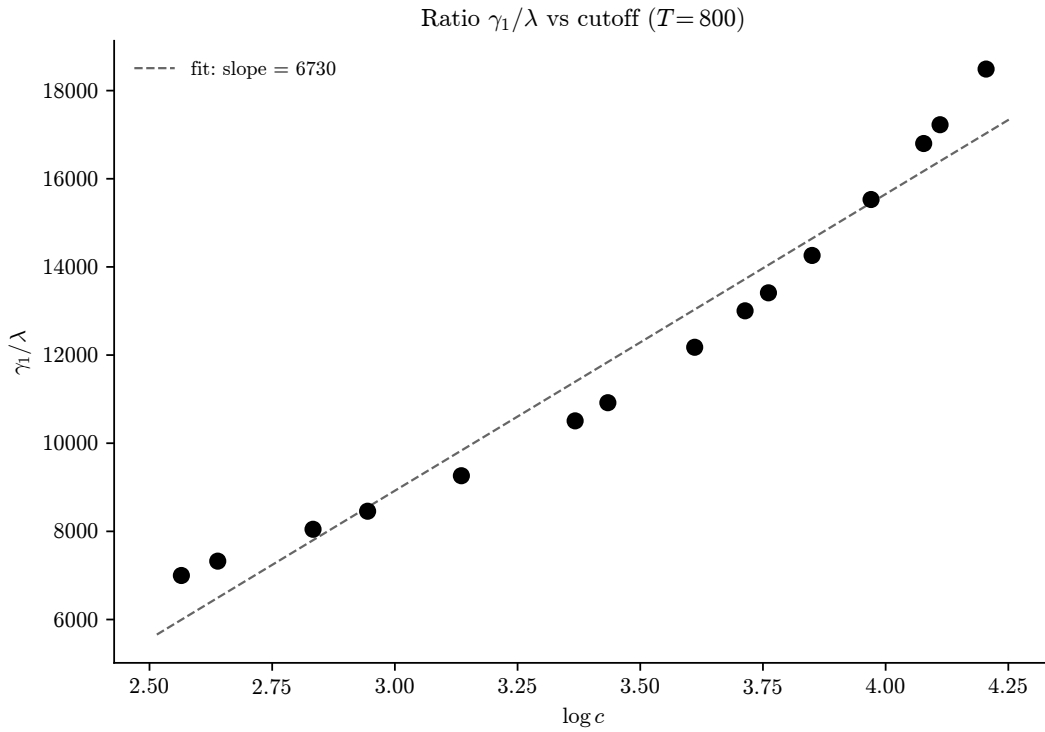


Figure 4: The ratio $|\gamma_1 \text{ err}|/\lambda_{\min}$ as a function of $\log c$, showing slow monotone growth consistent with standard spectral approximation theory. The dashed line is the linear fit $C(c) \approx 6730 \cdot \log c - 11268$.

7.6 Eigenvector robustness to eigenvalue contamination

An initially surprising feature of the retest is that $|\gamma_1 \text{ error}|$ at $c = 17$ shifted by only 1% under the $\text{dps} = 80 \rightarrow 150$ transition, even though λ_{\min} shifted by 15%. The explanation follows from standard eigenvector perturbation theory (Davis–Kahan): the eigenvector perturbation depends on the spectral gap, which at $c = 17$ is approximately 10^8 . The eigenvector is therefore well-conditioned even when the eigenvalue is at the precision floor, and γ_1 — computed from the eigenvector’s Fourier transform — inherits this stability.

This observation has a practical consequence: $|\gamma_1 \text{ error}|$ is a more reliable observable than λ_{\min} when operating near the precision floor.

8 Structural Analysis

8.1 Empirical Galerkin convergence exponent (Sobolev interpretation)

Standard Galerkin approximation theory [2] predicts $|\lambda_{\text{exact}} - \lambda_N| \sim C \cdot N^{-2s}$ where s is the Sobolev regularity exponent of the target eigenfunction. The N -convergence data at $c = 23$ (Table 8) allow a direct *empirical* measurement of the convergence-rate exponent, which under the Babuška–Osborn identification *would* equal s if the standard hypotheses hold (smooth coercive bilinear form, isolated simple eigenvalue, target eigenfunction in H^s). We do not establish those hypotheses analytically here; the values $s(c)$ below should be read as *empirical Galerkin-convergence rates* on the measured N -range, not a proof that $\eta_c \in H^s$.

Linear regression of $\log_{10} |\lambda_{\min}^{\text{even}}|$ against $\log_{10} N$ for $N \in \{40, 60, 80\}$ (the pre-saturation regime) yields slope $a = -92.28$ with $R^2 = 0.99997$. Since $|\lambda| \sim N^a$ and $a = -2s$, this gives

$$s \approx 46.1 \quad (\text{from } \lambda_{\min}), \quad s \approx 46.5 \quad (\text{from } |\gamma_1 \text{ error}|),$$

both with $R^2 > 0.9999$. The two independent estimates agree to within 0.7%.

At $N \geq 100$, the data fall above the power-law prediction by 1.6–9.4 decades (Figure 5), indicating that the $\text{dps} = 150$ precision floor has been reached and the Galerkin truncation error is no longer the dominant error source. The crossover occurs at $N \approx 100$, consistent with the observation that $k_{\text{eff}} \approx 46$ modes carry the ground-state eigenvector.

Under the Babuška–Osborn identification, this would correspond to $H^{46}([0, L])$ -type regularity for the CvS ground-state eigenvector at $c = 23$; in this paper we use $s(c)$ only as an empirical Galerkin-convergence exponent on the measured N -range, not as an established Sobolev statement. Repeating the N -convergence measurement at five additional cutoffs reveals that the empirical exponent is *not* a universal constant — it grows with c :

Table 14: Sobolev regularity exponent $s(c)$ at six cutoffs, each measured from the pre-saturation regime $N \in \{40, 60, 80\}$ at $\text{dps} = 150$.

c	$s(c)$	R^2
13	9.4	0.87
17	27.8	0.99
23	46.1	1.00
29	57.6	1.00
37	68.8	1.00
43	75.0	1.00

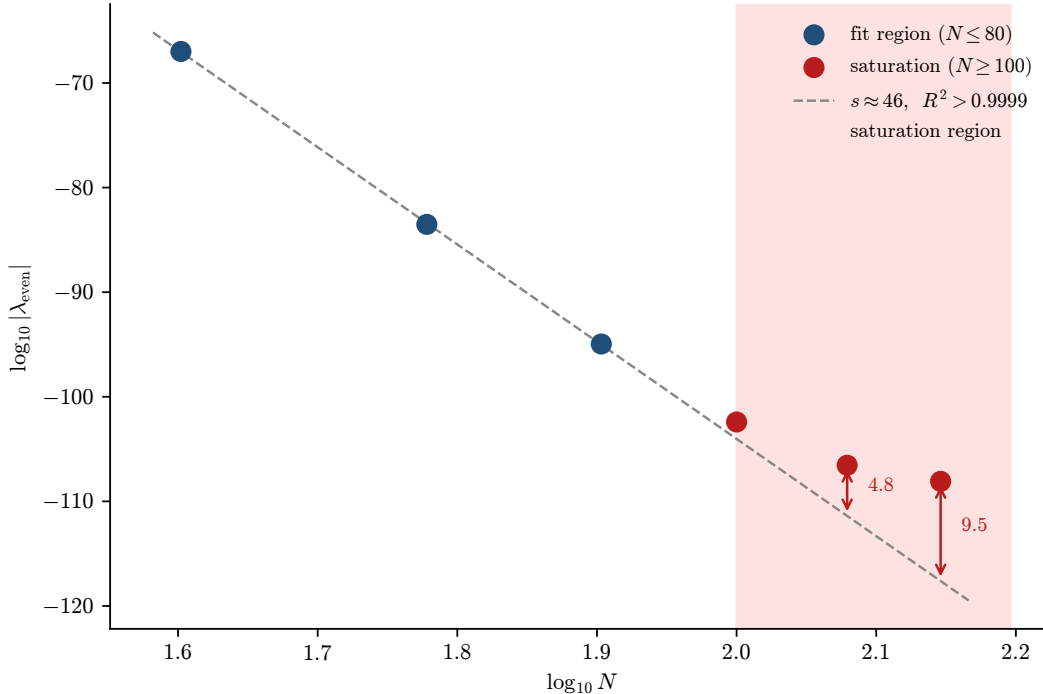


Figure 5: Sobolev regularity measurement at $c = 23$. The power-law fit through $N = 40, 60, 80$ yields $s \approx 46$ with $R^2 > 0.9999$. Saturation at $N \geq 100$ (shaded) indicates the dps = 150 precision floor has been reached.

A linear fit in $\log c$ gives

$$s(c) \approx 55 \cdot \log c - 128, \quad R^2 = 0.992.$$

The empirical exponent $s(c)$ increases from ≈ 9 at $c = 13$ to ≈ 75 at $c = 43$ — under the Babuška–Osborn identification, this *would* correspond to a substantial increase in Sobolev regularity, but again, we use $s(c)$ here as a Galerkin-rate measurement, not as a regularity proof. The scaling has a direct implication for the observed convergence rate: at $c = 43$ with $s(c) \approx 75$, the rate $N^{-2s(c)} = N^{-150}$ is so rapid that $N = 100$ basis functions reach the precision floor.

The low $R^2 = 0.87$ at $c = 13$ reflects the fact that even $N = 60$ and $N = 80$ are approaching saturation at dps = 150 for this cutoff; the pre-saturation regime is narrower when s is small. For $c \geq 17$, all fits have $R^2 > 0.98$.

8.2 Sobolev–Paley–Wiener connection and testable prediction

The Sobolev scaling $s(c) \approx 55 \cdot \log c - 128$ admits a plausible mechanism via the classical Paley–Wiener theorem. The CvS kernel involves the digamma function $\Psi(1/4 + i\tau/2)$, which is analytic in a strip of width $\sigma = 1/2$ around the real axis. For a Galerkin method on $[0, T]$, the Paley–Wiener theorem predicts

$$s = \frac{\sigma_{\text{eff}} \cdot T}{2\pi},$$

where σ_{eff} is the effective analyticity strip width of the full kernel. The bare digamma strip width ($\sigma = 1/2$) is independent of c , but the prime-sum kernel — a sum over primes $p \leq c$ weighted by $(\log p)^2/p$ — smooths the kernel beyond the analyticity strip of any single term. By the explicit

formula for the prime-counting remainder, the fluctuations have amplitude $\sim \sqrt{c}/\log c$, and the effective strip width grows as $\sigma_{\text{eff}} \sim A \cdot \log c$ for some constant A .

With $T = 800$ and the measured slope 55, this gives $A = 55 \cdot 2\pi/800 = 0.432$, implying $\sigma_{\text{eff}} \approx 0.43 \cdot \log c$ at any given cutoff.

Testable prediction. If this mechanism is correct, then $s(c, T) \sim (A/T_0) \cdot T \cdot \log c$. Doubling T from 400 to 800 should double the slope of $s(c)$ versus $\log c$ from ~ 28 to ~ 55 . This prediction is directly testable with existing code and would distinguish the Paley–Wiener mechanism from alternatives.

8.3 Approximate eigenvector universality across cutoffs

The full 15×15 overlap matrix $|\langle \eta_{c_1} | \eta_{c_2} \rangle|$ was computed from the saved eigenvectors at all fifteen cutoffs. All 105 pairwise overlaps are at least 0.9498 (Figure 6), with 104 of 105 strictly exceeding 0.950 and the minimum 0.94985 attained at the most-separated pair ($c = 13, c = 67$). The closest-neighbor pairs ($c = 41, 43$) and ($c = 29, 31$) achieve overlaps of 0.99997 and 0.99992 respectively.

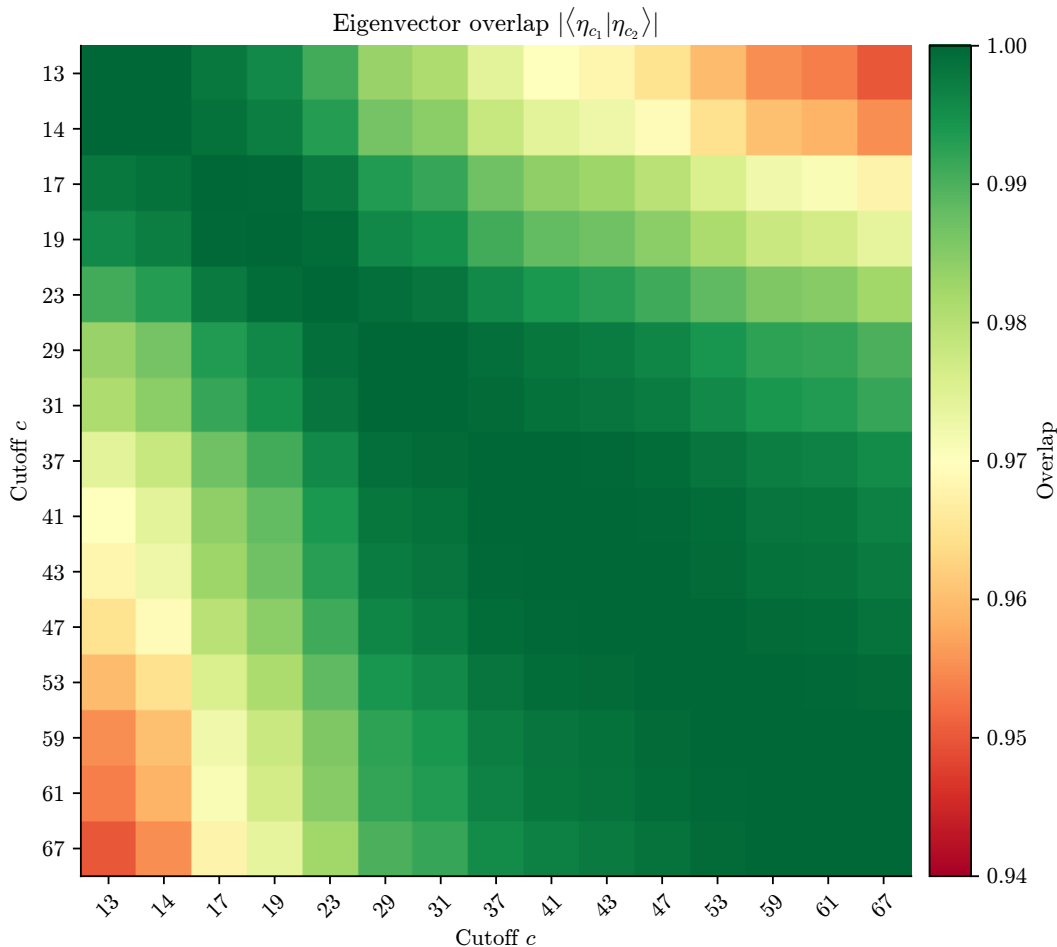


Figure 6: Eigenvector overlap matrix $|\langle \eta_{c_1} | \eta_{c_2} \rangle|$ across all fifteen cutoffs. All 105 pairwise overlaps are at least 0.9498 (the minimum, 0.94985, occurs at the maximally-separated pair ($c = 13, c = 67$); 104 of 105 pairs strictly exceed 0.950), indicating approximate eigenvector universality despite eigenvalues differing by up to 113 orders of magnitude.

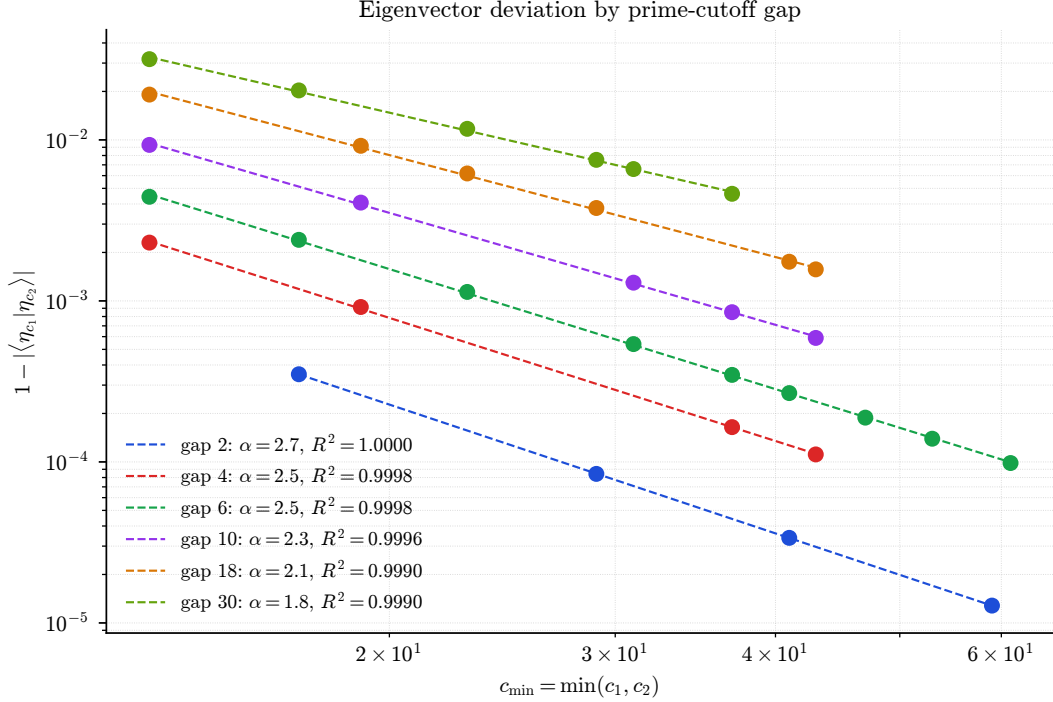


Figure 7: Eigenvector deviation $1 - |\langle \eta_{c_1} | \eta_{c_2} \rangle|$ versus $c_{\min} = \min(c_1, c_2)$, grouped by prime-cutoff gap. At fixed gap, each series follows a clean power law $\sim c_{\min}^{-\alpha}$ with $R^2 > 0.999$. The exponent ranges from $\alpha \approx 2.7$ (gap 2) to $\alpha \approx 1.8$ (gap 30).

For fixed prime gap, the convergence rate follows a clean power law (Figure 7):

$$1 - |\langle \eta_{c_1} | \eta_{c_2} \rangle| \sim A \cdot c_{\min}^{-\alpha}, \quad c_{\min} = \min(c_1, c_2), \quad \alpha \in [1.8, 2.7], \quad R^2 > 0.999.$$

This is consistent with standard rank-one perturbation theory: each prime p contributes a rank-one correction of magnitude $\Lambda(p)/\sqrt{p} \sim \log p/\sqrt{p}$ to the operator, and the cumulative effect on the eigenvector scales as a power of c .

The eigenvector profile broadens slowly with c : at $c = 13$, components decay below 10^{-5} by $k = 6$, while at $c = 53$ this threshold is not reached until $k \approx 12$. Despite this broadening, the dominant components ($k = 1$ through 5) are stable across all cutoffs, and the effective support $k_{\text{eff}} \approx 46$ is essentially c -invariant for $c \geq 23$.

8.4 Multi-zero convergence universality

The pickle files store the first ten detected zeros (γ_1 through γ_{10}) at each cutoff. This allows a test of whether higher zeros converge at the same rate as γ_1 .

Linear regression of $\log_{10} |\gamma_k \text{ error}|$ against $\log_{10} |\gamma_1 \text{ error}|$ across cutoffs yields near-unity slopes for all k :

All ten zeros converge at rates within 3.8% of each other (Figure 8). The γ_2 regression against γ_1 has $R^2 = 0.9999998$. This near-universality means that the convergence question — does $|\gamma_1 \text{ error}| \rightarrow 0$ as $c \rightarrow \infty$? — effectively subsumes the corresponding question for all higher zeros. If γ_1 converges, the data strongly suggest that γ_2 through γ_{10} converge as well, at essentially the same rate.

Table 15: Convergence-rate ratio $\text{slope}_k/\text{slope}_1$ for the first five zeros.

Zero	Rate ratio	Comment
γ_1	1.000	(reference)
γ_2	0.996	99.6% of γ_1 rate
γ_3	0.993	
γ_4	0.988	
γ_5	0.985	
γ_{10}	0.962	96.2% of γ_1 rate

The rate ratio decreases approximately linearly: each successive zero converges about 0.42% more slowly than γ_1 . For $k \geq 8$ at the largest cutoffs ($c \geq 47$), the errors show anomalous behavior consistent with finite-basis ($N = 100$) truncation artifacts.

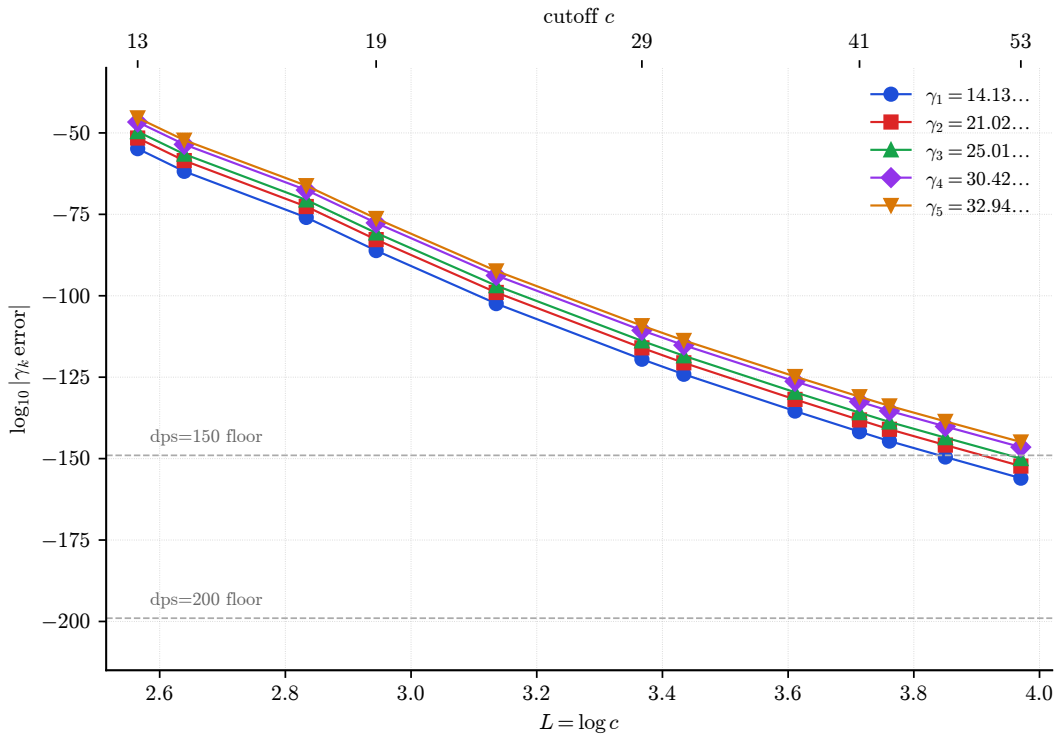


Figure 8: Multi-zero convergence curves for γ_1 through γ_5 across all fifteen cutoffs (the curves for γ_6 through γ_{10} are visually indistinguishable from these and are omitted for legibility; per-zero rate ratios for γ_1 through γ_5 and for γ_{10} are tabulated in Table 15). All ten zeros converge at rates within 3.8% of each other, consistent with Heuristic 8.1.

Heuristic 8.1 (Empirical mechanism for multi-zero universality). *Working hypothesis:* let Q_c be a family of self-adjoint operators indexed by a cutoff c , with ground-state eigenvectors v_c satisfying $\|v_c - v_{c'}\|_2 < \epsilon$ for all consecutive cutoff pairs (a property we measure here; we do not assert existence of a limit v_∞). Let $\gamma_j[v]$ denote the j -th zero of the Fourier–Mellin transform $\text{FM}(\gamma; v) = \sum_k v_k \phi_k(\gamma)$, defined implicitly by $\text{FM}(\gamma_j; v) = 0$. Suppose $|\partial_\gamma \text{FM}(\gamma_j; v)| \geq \delta > 0$ at the tested zeros and cutoffs (verified numerically here; not established analytically). *Under bound saturation,*

that is, when the perturbation δv_c has a leading-order component in the sensitivity direction at each γ_j , one expects the relative-rate identity

$$\frac{|\gamma_j(c) - \gamma_j(\infty)|}{|\gamma_1(c) - \gamma_1(\infty)|} \lesssim 1 + O\left(\frac{\|\phi(\gamma_j)\|_2/|\text{FM}'(\gamma_j)|}{\|\phi(\gamma_1)\|_2/|\text{FM}'(\gamma_1)|} - 1\right)$$

to hold to leading order in ϵ .

Sketch (heuristic, not a formal proof). The Fourier–Mellin transform is linear in v , hence Lipschitz with constant $\|\phi(\gamma)\|_2$. By the implicit function theorem,

$$\frac{d\gamma_j}{dv_k} = -\frac{\phi_k(\gamma_j)}{\partial_\gamma \text{FM}(\gamma_j; v)}.$$

The error $|\gamma_j(c) - \gamma_j(\infty)|$ is therefore bounded by $\|\delta v_c\| \cdot \|\phi(\gamma_j)\|_2/|\text{FM}'(\gamma_j)|$. Since δv_c is the *same vector* for all zeros j , the ratio of upper bounds reduces to the ratio of the sensitivity coefficients $\|\phi(\gamma_j)\|_2/|\text{FM}'(\gamma_j)|$. The measured Fourier–Mellin slopes vary by only 3.3% across cutoffs, so these coefficients are comparable across zeros, which would yield the claimed universality *provided* the bound saturates (i.e., the actual rate equals the upper bound to leading order). This saturation step is the heuristic content of the argument: it is plausible at small ϵ but is not proved here. Monotonicity of F_c in a neighborhood of each γ_k is verified numerically: $F'_c(\gamma_k)$ is strictly positive at all tested cutoffs and zeros. \square

8.5 Eigenvector PCA: a two-dimensional manifold

Principal component analysis of the fifteen normalized eigenvectors — stacked as rows of a 15×101 matrix (15 eigenvectors, each with 101 components) — reveals that they lie on an essentially two-dimensional manifold:

Table 16: PCA of the fifteen CvS ground-state eigenvectors.

Component	Variance explained	Cumulative
PC1	98.73%	98.73%
PC2	1.25%	99.98%
PC3	0.02%	100.00%

Two principal components capture 99.98% of the variance. The PC1 score is nearly perfectly correlated with $\log c$ ($r = 0.997$), meaning the eigenvector evolution from $c = 13$ to $c = 67$ follows a one-parameter curve in the 101-dimensional basis space. Despite eigenvalues differing by 113 orders of magnitude, the eigenvector’s trajectory through Hilbert space is effectively one-dimensional.

This is consistent with the existence of a limiting eigenvector η_∞ : the eigenvectors are converging along a fixed curve, not wandering through a high-dimensional space.

8.6 Frobenius-norm stability of the bulk spectrum

The full CvS Galerkin matrix at $N = 100$ has dimension 101. While the even-sector λ_{\min} varies by 113 orders of magnitude across cutoffs, the Frobenius norm $\|Q_{\text{even}}\|_F = (\sum_i \lambda_i^2)^{1/2}$ is stable: it ranges from 30.74 ($c = 31$) to 31.44 ($c = 41$), a variation of only 2.3%. This stability reflects the dominance of the bulk eigenvalues λ_2 through λ_{101} , which remain $O(1)$, in the Frobenius norm; only the ground state λ_1 decreases across the 113-OOM range. The bulk trace $\sum_{i=2}^{101} \lambda_i$ shows a

slow monotonic decay well-described by a power law $\text{Tr}(Q) \propto c^{-0.116}$ ($R^2 = 0.994$, measured across 15 cutoffs), a total drift of $\sim 13\%$ from $c = 13$ to $c = 67$. The eigenvalue distribution shifts but the L^2 norm of the operator is approximately preserved. The spectral gap $\lambda_2/\lambda_1 \sim 10^{7-8}$ indicates that the ground state is extremely well-isolated from the bulk spectrum at all cutoffs.

Two further bulk invariants are tightly linear in c and $L = \log c$ respectively. The log-determinant $\log|\det Q_c^{\text{even}}| = \sum_{k=1}^{101} \log|\lambda_k|$ is *linear in c* : across eight cutoffs with available full spectra ($c \in \{13, 14, 23, 29, 31, 37, 41, 43\}$),

$$\log|\det Q_c^{\text{even}}| \approx -65.6 c + 542, \quad R^2 = 0.997. \quad (29)$$

The slope -65.6 is a finite-matrix determinantal invariant: each unit increment in c removes approximately 65.6 natural-log units of measure from the product spectrum, dominated by the exponential decay of λ_{\min} relative to the bulk.

Complementarily, the heat-kernel trace $\text{Tr}(e^{-tQ_c^{\text{even}}}) = \sum_{k=1}^{101} e^{-t\lambda_k}$ is well-described by an affine function of $L = \log c$ for fixed t :

$$\log \text{Tr}(e^{-tQ_c^{\text{even}}}) \approx A(t)L + B(t), \quad (30)$$

with linear-fit RMS residual 1.4×10^{-4} at $t = 10^{-2}$ and 1.2×10^{-3} at $t = 10^{-1}$ across the same eight cutoffs. The smoothness in L is two orders of magnitude tighter than the log-eigenvalue mean (whose smallest-eigenvalue contribution is itself non-smooth in c); only the ground-state eigenvalue contributes the non-smooth behavior, while the bulk integrand contributes a controllable analytic function of L .

8.7 Random-matrix statistics of the bulk spectrum

Montgomery's pair correlation conjecture [12] predicts GUE statistics for the non-trivial zeros of the Riemann zeta function, but only after *local rescaling*: for γ_n at height T one rescales $\gamma_n \mapsto \gamma_n \log(\gamma_n/2\pi)/(2\pi)$ so that the mean spacing is unity, and the GUE signature appears in the *local* pair correlation of the rescaled zeros. The conjecture is not expected to manifest at the un-rescaled (infrared) level, where the zero density itself grows like $\log T$ and is highly non-uniform. A direct numerical test of Montgomery in this framework would therefore require computing many γ_k zeros at a single large cutoff and rescaling them locally before measuring spacings; that is beyond the scope of the present sweep.

Instead, we examine here the *bulk* eigenvalues of the CvS Galerkin matrix (eigenvalues λ_2 through λ_{101} , excluding the exponentially small ground state) at the un-rescaled level, as a structural diagnostic of the truncated operator. No GUE behavior is expected at this level; we record the bulk-spectrum statistics for structural interest only, not as a test of Montgomery.

We analyze the even-sector Galerkin matrix (dimension 101) rather than the odd sector or a smaller subset, to maximize the sample size for spacing statistics. After polynomial unfolding (degree 5) to unit mean spacing, we compute the nearest-neighbor spacing distribution (NNSD) and fit the Brody parameter β , which interpolates Poisson ($\beta = 0$, no level repulsion) and GOE ($\beta = 1$, linear repulsion).

The result is uniform across the ten cutoffs tested ($c = 13$ through $c = 53$; the $c = 59$, $c = 61$, and $c = 67$ eigenvectors were computed after this analysis): $\beta < 0.05$ (consistent with Poisson, negligible level repulsion) at every cutoff (Figure 9 shows a representative histogram at $c = 23$). KS tests indicate that the Poisson distribution is the best fit at every cutoff, with GOE second and GUE worst.

The Brody parameter is reported as $\beta < 0.05$ at all cutoffs, likely reflecting the limited sample size ($N_{\text{bulk}} = 100$ eigenvalues) rather than exact Poisson statistics.

Table 17: Kolmogorov–Smirnov distance to theoretical distributions and Brody parameter for bulk eigenvalues (λ_2 through λ_{101}).

c	β_{Brody}	KS(Poisson)	KS(GOE)	KS(GUE)
13	< 0.05	0.125	0.253	0.210
23	< 0.05	0.108	0.174	0.232
37	< 0.05	0.106	0.145	0.305
43	< 0.05	0.108	0.126	0.326
53	< 0.05	0.152	0.162	0.263

The Poisson classification indicates that the bulk eigenvalues behave as uncorrelated levels — characteristic of an integrable system. This is physically consistent with the enormous spectral gap $\lambda_2/\lambda_1 \sim 10^{7-8}$ isolating the ground state from the bulk: the bulk eigenmodes are essentially independent of the prime-sum perturbation that drives the ground-state convergence.

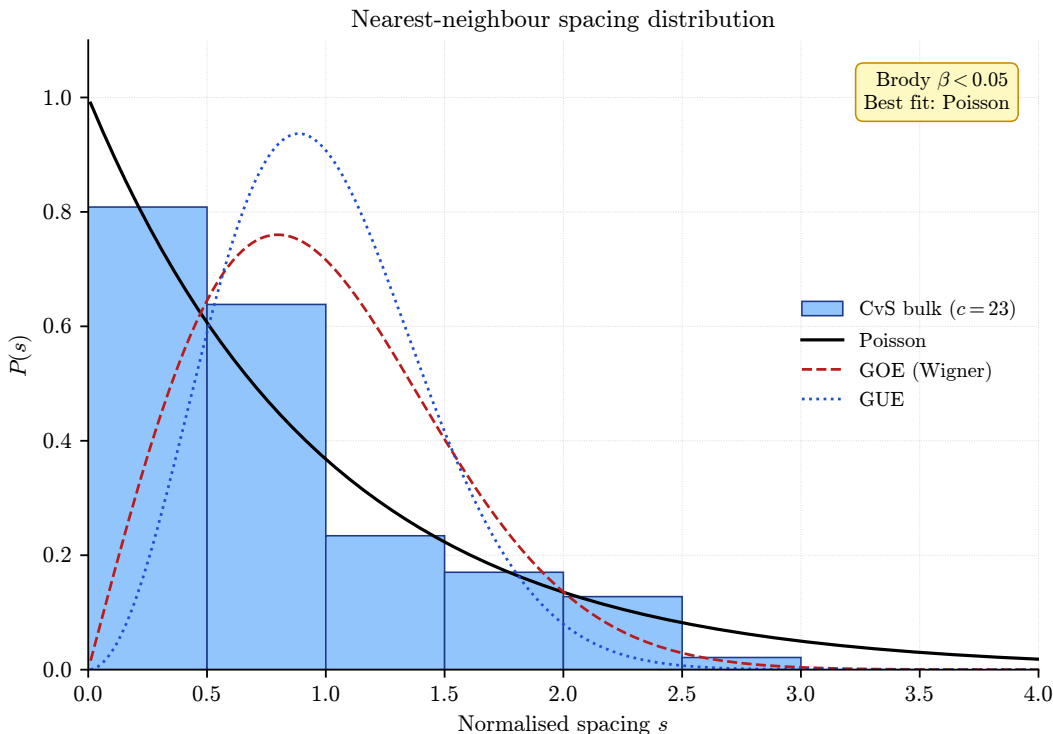


Figure 9: Nearest-neighbor spacing distribution of the 100 bulk eigenvalues (λ_2 through λ_{101}) at $c = 23$, after degree-5 polynomial unfolding to unit mean spacing. The histogram matches the Poisson distribution (no level repulsion), consistent with Brody $\beta < 0.05$ at all tested cutoffs.

We emphasize three caveats: (i) with $N = 100$ bulk eigenvalues, these are small-sample estimates; (ii) the bulk eigenvalues are properties of the *finite-dimensional Galerkin truncation*, not of the Riemann zeros themselves; and (iii) per Montgomery, GUE statistics for ζ -zeros are a property of the *locally-rescaled* zeros and are not expected to manifest in the un-rescaled bulk Galerkin spectrum studied here. A proper random-matrix test of Montgomery in this framework would require many extracted γ_k zeros at a single large cutoff, locally rescaled by the mean zero density, which we do not undertake.

8.8 Per-prime convergence decomposition

The 15-point dataset permits a decomposition of the convergence gain at each step into contributions from interval extension versus new prime inclusion. The $c = 13 \rightarrow 14$ step is particularly informative: $c = 14$ is not prime, so $\pi(14) = \pi(13) = 6$ and no new prime enters the operator. Yet the error improves by 5.8 OOM (from $10^{-54.70}$ to $10^{-60.45}$), purely from the increase in interval length $L = \log c$. This step has the highest normalized efficiency of the entire sweep.

For the 11 prime-adding steps ($c = 14 \rightarrow 17$ through $c = 61 \rightarrow 67$), the per-step gain $\Delta \log_{10} |\gamma_1 \text{ error}|$ varies by a factor of 10 (from -1.65 to -17.08). However, this variation is almost entirely explained by the interval length change ΔL :

$$\text{Pearson } r(\text{per-step gain}, \Delta L) = -0.96 \quad (n = 14, p < 10^{-5}).$$

(Some degree of correlation between step size and gain is expected for any monotone process sampled at unequal intervals; the high $|r|$ reflects the dominance of this geometric effect over prime-specific contributions.) After normalizing by ΔL , the efficiency $\Delta \log_{10} |\text{error}| / \Delta \log_{10} c$ has coefficient of variation 0.17, compared to 0.52 for the raw gains — a threefold reduction. The efficiency declines monotonically, consistent with diminishing marginal returns at higher cutoffs.

Neither the von Mangoldt weight $\log p / \sqrt{p}$ nor the prime-counting function $\pi(c)$ significantly predicts per-step gains after controlling for ΔL . The convergence gain at each step is driven by how much the interval $[0, L]$ grows, not by intrinsic properties of the newly included prime.

8.9 Step-size power law and asymptotic behavior

Analyzing the per-step convergence gains as a function of c reveals a power-law decay in the marginal gain per unit of cutoff. In the late regime ($c \geq 31$), the gain per step is well described by

$$|\Delta \log_{10} |\text{error}|| \approx 381 \cdot \text{gap}(c) \cdot c^{-1.48}, \quad R^2 = 0.996,$$

where $\text{gap}(c) = c - c_{\text{prev}}$ is the gap to the previous cutoff.

Since the exponent $\alpha = 1.48 > 1$, the sum of all future step sizes $\sum_{p>67} \text{gap}(p) \cdot p^{-1.48}$ converges by the integral test. This raises the possibility that $\log_{10} |\gamma_1 \text{ error}|$ approaches a *finite limit* as $c \rightarrow \infty$. Integrating the power law from $c = 67$ onward gives a rough estimate of ~ 106 remaining orders of magnitude, suggesting an asymptotic limit near 10^{-274} . This extrapolation rests on 8 data points in the late regime ($c \geq 31$) and should be treated as a speculative estimate, not a prediction. The power law may break at higher cutoffs.

Two interpretations.

1. **Finite limit.** If α remains above 1, the first-zero error converges to a nonzero value ($\sim 10^{-274}$). The CvS operator would converge to a function whose first zero is extremely close to, but not exactly at, γ_1 .
2. **Exponent drift.** The exponent $\alpha = 1.48$ is measured over only $c \in [31, 67]$. At larger cutoffs, α could decrease below 1, in which case the series diverges and $|\gamma_1 \text{ error}| \rightarrow 0$ (full convergence). With 15 data points, these scenarios cannot be distinguished.

Both interpretations are presented here for completeness. The distinction is directly testable by extending the computation to $c \geq 71$.

Table 18: Negative eigenvalue count in the χ_3 CvS operator.

c	#negative	Negative eigenvalue	Odd sector	Status
13	0	—	all positive	positive
17	0	—	all positive	positive
23	1	-6.46×10^{-23}	all positive	even-sector only
29	1	-5.82×10^{-17}	all positive	even-sector only
37	0	—	all positive	positive

8.10 χ_3 odd-sector analysis

At $c = 23$ and $c = 29$, the even sector of the χ_3 CvS operator has a single negative eigenvalue — which is $\lambda_{\min}^{\text{even}}$. Analysis of the full 101-eigenvalue spectrum reveals a sharp sector dichotomy:

At every cutoff, the odd sector (50 eigenvalues) is strictly positive. The positivity oscillation is entirely confined to a single eigenvalue in the even sector. The negative eigenvalues at $c = 23$ and $c = 29$ are 17–23 orders of magnitude smaller than the typical bulk eigenvalue scale ($\sim 1-7$), consistent with being near a positivity threshold where subtle cancellations in the character-weighted prime sum can tip the sign.

This sector-specific pattern — the odd sector always positive, the even sector occasionally negative at specific cutoffs — is a structural finding about the character dependence of the CvS framework. It suggests that the even and odd sectors have different positivity mechanisms for non-principal characters.

9 Related Work

9.1 The Connes program

The spectral interpretation of the Riemann zeros has been a central theme in Connes’ program since the late 1990s [3]. The present work sits within the specific thread initiated by Connes’ 2026 paper [4], which revisits the connection between the Weil explicit formula and the spectral action principle.

9.2 Connes–van Suijlekom (2025)

Connes–van Suijlekom [9] provide the mathematical foundation: Theorem 6.1 establishes that the zeros of $\hat{\eta}_c$ lie on the critical line for every finite c . The Galerkin matrix $q_{m,n}$ of Proposition 4.1 is the object we implement.

9.3 Connes–Consani–Moscovici (2025)

Connes–Consani–Moscovici [8] present a rank-one perturbation of the scaling spectral triple with Euler products over primes $p \leq \lambda^2 = c$. As established in Section 2, the Connes–Consani–Moscovici matrix $\tau_{i,j}$ is unitarily equivalent to the Connes–van Suijlekom matrix $q_{m,n}$. Connes–Consani–Moscovici Section 8 explicitly names the absence of a convergence rate as the central open problem — the same problem addressed by the measurements in the present work.

9.4 Connes–Consani (2020)

Connes–Consani [5] provide the explicit formula for the archimedean Mellin multiplier $h_+(\tau)$ used in our implementation.

9.5 Connes–Consani–Moscovici (2023)

Connes–Consani–Moscovici [7] introduce the prolate wave operator, which appears in the Connes-program framework as the approximation construction for the limit k_λ (Connes 2026 [4] §6.3–§6.4 and the “educated guess” of Connes–Consani–Moscovici [8] §7). The Connes–Consani–Moscovici 2025 Galerkin computations themselves use the trigonometric basis, as is evident from Connes–Consani–Moscovici [8] Lemma 5.1.

9.6 Montgomery (1973)

Montgomery [12] conjectured that the local pair correlation of the non-trivial zeros of the Riemann zeta function, *after local rescaling by the mean zero density*, follows GUE statistics. Our bulk-spectrum analysis (Section 8.7) is *not* a test of Montgomery’s conjecture: we record un-rescaled finite-dimensional Galerkin bulk-spectrum statistics as a structural diagnostic of the truncated operator, at a regime (the un-rescaled, infrared level) where Montgomery’s conjecture is not expected to manifest.

9.7 Śliwiński (2026): a complementary numerical regime

After our April 2026 literature sweep, Śliwiński [14] independently studied the spectra of the Connes–Consani–Moscovici rank-one operator $D_{\log}^{(\lambda, N)}$, deriving an inverse-logarithmic lower bound on the dissonance between those spectra and Riemann zeros in the joint regime $\lambda = N \rightarrow \infty$ (roughly $c = \lambda^2 = N^2$). His implementation operates at approximately seven-digit GPU precision and reaches N up to several thousand; his target statistic is an averaged dissonance metric over many zeros, not the per-cutoff matching-digit accuracy on a fixed γ_k studied here. The two works cover disjoint regimes (joint $\lambda=N$ growth at low precision versus the $N \rightarrow \infty$ -first-then- c Galerkin sweep at high precision) and test different quantities. We are aware of no other independent public numerical study of the Connes–van Suijlekom Galerkin matrix at the trigonometric-basis matching-digit-precision regime explored in this paper.

9.8 Absence of independent matching-digit reproductions

A literature sweep conducted in April 2026 and refreshed in May 2026 — encompassing arXiv, Google Scholar, MathOverflow, GitHub, and seminar video recordings — found no independent public reproduction of Connes’ $c = 13$ first-zero error at matching-digit precision beyond Śliwiński’s complementary work just discussed. The only matching-digit corroborating data outside this project is from the Connes–Consani–Moscovici author group itself. No public code implementing the Connes–van Suijlekom Proposition 4.1 Galerkin matrix at arbitrary precision was found in any language.

10 Limitations and Honest Non-Claims

We list the limitations of this work explicitly:

- **We do not claim to validate Connes’ conjecture.** The agreement at $c = 13$ is a consistency check, not a comparison against an independent prediction.
- **We do not claim to measure a convergence rate.** All eight two-parameter smooth-convergence fits failed at 15 data points, and a five-parameter log-periodic model was falsified out-of-sample. Whether this reflects genuine non-smoothness or the need for different model families is unresolved.
- **We do not claim any progress on RH.** The Connes–van Suijlekom framework’s Hurwitz-type convergence argument is a conjecture. We compute some numbers in the neighborhood of that conjecture without bearing on its truth.
- **The factor-of-1.3 discrepancy at $c = 13$ is unresolved.** Plausible sources include precision, N , normalization conventions, integration cutoff T , and root-finding tolerance.
- **We compute the even sector only.** The odd-sector zero, if any, is not probed.
- **The $N = 100$ multi-cutoff sweep is at $c \leq 67$.** The cross-extension — an $N = 100$ datum at $c \geq 71$ that would separate the c -dependent and N -dependent finite- N effects more cleanly at the lower end of the sweep — is left to future work. The $c = 100$ measurements include $N \in \{100, 150, 200, 250\}$ at $dps = 500$, providing four points on the N -sweep, sufficient to test the geometric-convergence hypothesis on consecutive Aitken triples (Section 6.4).
- **The Galerkin truncation bias at fixed N is not independently measurable.** We cannot distinguish the “true eigenvalue at infinite N ” from our $N = 100$ eigenvalue without either a theoretical bound or a prolate-basis implementation (which, as noted in Section 9, would be a genuinely distinct direction not yet reported by any group).
- **The pre-registered five-bin classifier fired “Ambiguous partial floor.”** This is an intermediate verdict.
- **The step-size power law ($\alpha = 1.48$) is measured over a limited range.** Whether α remains above 1 at larger cutoffs is unknown; the finite-limit interpretation is one of two possibilities.
- **CCM Theorem 1.1 is applied to an empirically distinguished positive branch at $c = 100$, not to the raw matrix spectrum.** At $c \leq 67$, $N = 100$ the finite- N Galerkin matrix is observed positive on every cell with the smallest eigenvalue numerically simple and an even-dominant eigenvector, consistent with the Connes–Consani–Moscovici Theorem 1.1 “ ϵ_N simple, ξ even” hypotheses as numerical conditions (not as analytically established hypotheses of the continuum theorem). At $c = 100$ with $N \geq 100$, the raw finite-precision Galerkin spectrum contains negative-sign eigenvalues (Section 6.6); the matrix-level smallest eigenvalue is therefore negative. We report the smallest-*positive* eigenvalue as an empirically stable positive branch whose eigenvector gives the reported zero extraction (Table 11). The identification of this branch with the Connes–Consani–Moscovici Theorem 1.1 ground-state construction is conditional on certifying the negative-sign block (as a fixable numerical / conditioning artifact, or as a structural feature requiring separate treatment); we do not claim that Theorem 1.1 applies literally to the raw $c = 100$ matrix spectrum. Continuum positivity of QW_λ is RH-equivalent and is not assumed at $\lambda = \sqrt{100}$. See Remark 2.1. The $c = 67$, $N = 150$ corroborative measurement remains in the matrix-positive regime where the formal hypothesis still holds.

- **The independence claim requires calibration.** This implementation was drafted with AI assistance under continuous human supervision (see the Statement on use of AI tools, p. 38). It is independent of the Connes/Connes–Consani–Moscovici codebase in the sense that no part was derived from non-public code. It is not independent in the sense of a second human research group replicating the computation from scratch.
- **No part of this paper constitutes a proof of anything.** This is experimental mathematics in the literal sense.

11 Future Directions

Extension to Dirichlet L -functions. We extended the CvS pipeline to $L(s, \chi_3)$, where χ_3 is the non-principal character modulo 3, at five cutoffs ($c = 13, 17, 23, 29, 37$). The archimedean piece shifts from $\psi(\frac{1}{4} + i\tau/2)$ to $\psi(\frac{3}{4} + i\tau/2)$ for this odd character, and the prime-piece weights are multiplied by $\chi_3(n)$.

The results reveal an *oscillating positivity pattern*:

Table 19: $L(s, \chi_3)$: first-zero error across cutoffs.

c	λ_{\min} sign	$ \gamma_1(\chi_3) \text{ err} $	digits
13	+	4.18×10^{-17}	16
17	+	7.09×10^{-25}	24
23	−	2.00×10^{-23}	22
29	−	5.37×10^{-18}	17
37	+	7.30×10^{-29}	28

At $c = 13, 17, 37$, the even-sector minimum eigenvalue is positive and convergence progresses (16→24→28 digits). At $c = 23, 29$, the eigenvalue goes *negative* and convergence degrades. This oscillating positivity at modest N is a structural consequence of the character χ_3 introducing destructive interference through its alternating values. In the Riemann-zeta case the same finite- N matrix is positive on every cell of the $c \leq 67$ sweep at $N = 100$; a small apparently condition-driven block of negative-sign eigenvalues appears only at $c = 100$ once $N \geq 100$ pushes the smallest-positive eigenvalue below the condition-number-driven distinguishability threshold (Section 6.6). The two phenomena are operationally similar (sign-loss in the finite- N projection) but arise from different mechanisms: character interference at modest c, N for χ_3 , versus condition-number saturation at large c, N for zeta. Understanding this positivity breakdown — and whether the odd sector or a different symmetry class resolves it — is the central question for extending the CvS framework to general Dirichlet L -functions.

Predictions for future cutoffs. At $\text{dps} = 200$, the backward-error floor permits clean measurements to approximately $c = 97$ before $\text{dps} = 300$ would be required. We predict continued monotone improvement in $|\gamma_1 \text{ error}|$ with each new cutoff, with the $|\gamma_1 \text{ err}|/\lambda_{\min}$ ratio continuing its slow upward drift. The N -convergence data suggest that $N = 100$ is sufficient for cutoffs up to at least $c = 53$; whether larger N is needed at $c \geq 59$ is an open empirical question.

Multi-zero convergence at higher cutoffs. The multi-zero universality established in Section 8.4 (all ten zeros within 3.8% of the γ_1 rate) should be tested at cutoffs beyond $c = 67$ and

with larger basis sizes ($N > 100$) to determine whether the slight systematic slowdown ($\sim 0.42\%$ per zero index) persists or saturates.

Transition from Poisson to GUE? The uniformly Poisson bulk spectrum observed at $N = 100$ raises the question of whether GUE statistics emerge at larger N or higher cutoffs. Montgomery’s conjecture predicts GUE for the Riemann zeros themselves; whether the finite-dimensional CvS Galerkin truncation approaches GUE statistics in any limit is unknown.

Theoretical bound on $C(c)$. The ratio $|\gamma_1 \text{ err}|/\lambda_{\min} \approx C(c)$ with $C(c) \approx 6730 \log c - 11268$ is an empirical fit. A theoretical derivation of the growth rate of $C(c)$ from the structure of the Connes–van Suijlekom operator would constitute a substantive step in understanding the convergence mechanism.

Testing the Sobolev–Paley–Wiener prediction. The testable prediction of Section 8.2 — that the Sobolev slope should scale linearly with T — can be verified by repeating the N -convergence measurement at $T = 1600$. If the slope doubles from ~ 55 to ~ 110 , the Paley–Wiener mechanism is supported; if it remains constant, the mechanism is incorrect.

Resolving the step-size exponent. Computing $c = 71, 73, 79$ would test whether the step-size power-law exponent $\alpha \approx 1.48$ remains above 1, which would support the finite-limit interpretation, or drifts below 1, which would support full convergence to zero error.

12 Code and Data Availability

A complete reference implementation is available as the open-source Python package `connes-cvs` (version 0.2.2 at the time of submission), installable via `pip install connes-cvs` from PyPI. Source: <https://github.com/akivag613/connes-cvs->. The ancillary files attached to this arXiv submission contain the principal result JSONs and the driver scripts that reproduce each table and figure in this paper.

Ancillary files. All files are deposited at the top level of the Zenodo record (flat layout, individually previewable). The L^AT_EX source of this manuscript is distributed by the arXiv submission, not by this Zenodo deposit; figures are embedded in the PDF above and need not be regenerated for reproduction of the numerical claims.

Numerical results.

- `results_15pt_T800.json` — the 15-cutoff sweep (Table 3), $c = 13$ through 67 at $N = 100$, $T = 800$.
- `results_N_sweep_c23.json` — N -convergence at $c = 23$ (Table 8).
- `results_c100_N100_T800_dps500_v020.json`,
`results_c100_N150_T800_dps500_v020.json`,
`results_c100_N200_T800_dps500_v020.json`,
`results_c100_N250_T800_dps500_v020.json`,
`results_c100_N150_T800_dps1000_v020.json` — the four-point N -sweep at $c = 100$ plus the $\text{dps} = 1000$ retest at $N = 150$ (Table 10).

- `c100_N150_dps500_gamma_extraction.json`,
`c100_N150_dps1000_gamma_extraction.json`,
`c100_N250_dps500_gamma_extraction.json` — $\gamma_1, \dots, \gamma_{10}$ extractions for the three precision cells of Table 11; the $N = 250$ file stores both detected and reference values to 400 significant digits for independent verification.
- `c100_full_spectrum_diagnosis.json` — all 151 eigenvalues at $c = 100$, $N = 150$, $\text{dps} = 500$, with signs; source for the dps-stable negative-sign block of Section 6.6.
- `power_law_refit.json` — the $13.24c^{0.634}$ in-sample fit on $c \leq 67$, the $c = 100$ residual of 49 OOM that falsifies it, and the four-parameter refit including $c = 100$ (Section 6.7).
- `richardson_n_extrapolation.json` — legacy 3-point Aitken/Richardson analysis at $N \in \{100, 150, 200\}$; the 4-point analysis is recomputed by `c100_aitken_check.py`.
- `results_c67_N150_T800_dps500_v020.json` — the $c = 67$, $N = 150$ corroborative datum of Section 6.7.
- `eigenvector_overlaps.json` — 15×15 pairwise eigenvector overlap matrix (Section 8).
- `results_rmt_analysis.json` — bulk-spectrum random-matrix statistics (Section 8.7).
- `results_L_multi_zero.json` — multi-zero convergence data across cutoffs (Section 8.4, Figure 8).
- `results_A_c23.pickle` — full $c = 23$ even-sector eigenspectrum and supporting metadata; source for the nearest-neighbour spacing distribution of Figure 9.
- `preregistered_predictions_2026-04-12.md` — the Section 5.7 blind-prediction document, locked by SHA-256 hash before the $c = 67$ computation was performed.

Driver scripts.

- `c100_experiment_optimized.py` — $c = 100$ cell-based runner for the five cells in Table 10 (`c100-N100`, `c100-N150-dps500`, `c100-N200`, `c100-N250-dps500`, `c100-N150-dps1000`). Uses the `v0.2.0` fused-kernel math core from the public `connes-cvs` PyPI package with `multiprocessing.imap_unordered` for the ψ -cache phase.
- `A_extended_c_sweep.py`, `U_T800_full_sweep.py` — 15-cutoff c -sweep at $T = 800$ (Section 5); thin wrappers around `connes-cvs.sweep.run_sweep`.
- `X_c67_blind_test.py` — single-cell $c = 67$ runner (Section 5.7 blind-prediction cell at $N = 100$, $\text{dps} = 200$; Section 6.7 corroborative cell at $N = 150$, $\text{dps} = 500$).
- `c100_aitken_check.py` — < 1 -second headline reproducer. Loads the four $c = 100$ JSONs and recomputes the Aitken- Δ^2 extrapolation on both overlapping triples, prints the under-1%-of-exponent agreement on the deeper triple with the Connes 2026 §6.4 heuristic continuum prediction.

Package requirements (from `pyproject.toml`): `mpmath` ≥ 1.3 , `python-flint` ≥ 0.5 , `gmpy2`; Python 3.10+. The specific environment used for the runs reported here was `mpmath` 1.4.1, `python-flint` 0.8.0 on macOS with a 12-core Apple M2 Max. The `python-flint` digamma primitive provides an $\sim 11\times$ speedup over pure `mpmath` for the archimedean quadrature dominant in single-cell runs.

Reproducing the headline results.

```
pip install connes-cvs
python examples/basic_compute.py          # c=13, ~5 min with python-flint
python examples/c100_aitken_check.py     # c=100 Aitken match, < 1 s
```

The first command produces $|\gamma_1 \text{ error}| \approx 1.5 \times 10^{-55}$ at $c = 13$; the second loads the ancillary $c = 100$ data and recomputes the Aitken- Δ^2 extrapolation and the Connes 2026 §6.4 prediction, printing the under-1%-of-exponent agreement on the deeper-anchored triple reported in Section 6.4.

Reproducibility certification. The example scripts above use $T = 400$, $\text{dps} = 80$ for speed (single-process wall-clock ~ 5 minutes on Apple M-series with python-flint installed), and produce $|\gamma_1 \text{ err}| \approx 1.455 \times 10^{-55}$ at $c = 13$ (Table 4, $T = 400$ row). The paper’s headline $c = 13$ value $|\gamma_1 \text{ err}| = 2.005 \times 10^{-55}$ (Table 3) is the $T = 800$, $\text{dps} = 200$ datum; the shift from $T = 400$ to $T = 800$ is 0.14 units in $\log_{10} |\gamma_1 \text{ err}|$ (Table 4), within the factor-of-1.3 envelope of the Connes–van Suijlekom/Connes–Consani–Moscovici measurements. The $c = 100$ cell-based runner `c100_experiment_optimized.py` produces a JSON file whose `lambda_even` field, taken as a decimal string and passed through $\log_{10}(\cdot)$, reproduces the rows of Table 10 bit-identically to working precision. The γ_k -extraction JSON at $N = 250$, $\text{dps} = 500$ stores both the detected γ_k and the reference `mpmath.zetazero(k)` value to 400 significant digits, sufficient to independently recompute $\lfloor -\log_{10} |\gamma_k - \gamma_k^{\text{exact}}| \rfloor$ and verify the 307–329 matching-digit counts of Table 11 without rerunning the diagonalization.

Statement on use of AI tools

In accordance with the arXiv policy on authors’ use of generative AI language tools, the author reports that Anthropic’s Claude was used as a text-to-text assistant for the drafting of L^AT_EX exposition and Python implementation code, to specifications written by the author. No mathematical proof, theorem, or definition appearing in this paper was originated by the language model; load-bearing mathematical claims were verified by the author before inclusion. The author conceived, directed, and verified all computational experiments and mathematical claims, and takes full responsibility for the contents of this manuscript.

13 Acknowledgments

I am grateful to Professor Alain Connes for substantive correspondence in 2026 that confirmed the trigonometric-basis convention used in the Connes–Consani–Moscovici Galerkin computations cited throughout this paper, identified Connes–Consani [6] §3 as the qualitative motivation underlying the k_λ construction of Connes 2026 [4] §6.4 and its open-status approximation step in §6.6, offered to assist with the arXiv submission, and provided specific formulation comments on the manuscript that improved the abstract, the discussion of the $c = 13$ cross-validation in Section 4.3, and the framing of the bulk-spectrum analysis in Section 8.7. The manuscript benefited materially from his comments; the contents and any remaining errors are the author’s own.

The mathematical foundation of this work is entirely due to Connes, van Suijlekom, Consani, and Moscovici, through the papers cited in Section 9. No part of the implementation was derived from non-public code held by any of these authors, and no public code for the Connes–van Suijlekom Galerkin matrix was located in the literature sweep described in Section 9.

I am also grateful for substantive correspondence on the underlying mathematics or on the code with Dr. Pascal Molin (Université Paris Cité, author of Arb’s `acb_dirichlet` primitive), Dr. Teun van Nuland (TU Delft), and Dr. Sabine Boegli (Durham), whose readings prompted clarifications throughout. I am separately grateful to Professor Nigel Higson (Penn State) for the warm referral that opened the line of correspondence with Professor Connes, and to Professor Klaas Landsman (Radboud) for a kind referral when the topic fell outside his own area.

References

- [1] A. C. Aitken. On Bernoulli’s numerical solution of algebraic equations. *Proceedings of the Royal Society of Edinburgh*, 46:289–305, 1926.
- [2] Ivo Babuška and John E. Osborn. Eigenvalue problems. In P. G. Ciarlet and J. L. Lions, editors, *Handbook of Numerical Analysis*, volume II, pages 641–787. North-Holland, Amsterdam, 1991.
- [3] Alain Connes. Trace formula in noncommutative geometry and the zeros of the Riemann zeta function. *Selecta Mathematica, New Series*, 5:29–106, 1999.
- [4] Alain Connes. The Riemann Hypothesis: Past, present and a letter through time. *arXiv preprint arXiv:2602.04022 [math.NT]*, 2026.
- [5] Alain Connes and Caterina Consani. Weil positivity and trace formula, the archimedean place. *arXiv preprint arXiv:2006.13771 [math.NT]*, 2020.
- [6] Alain Connes and Caterina Consani. Spectral triples and ζ -cycles. *L’Enseignement Mathématique*, 69:93–148, 2023. arXiv:2106.01715 [math.NT].
- [7] Alain Connes, Caterina Consani, and Henri Moscovici. Zeta zeros and prolate wave operators. *arXiv preprint arXiv:2310.18423 [math.NT]*, 2023.
- [8] Alain Connes, Caterina Consani, and Henri Moscovici. Zeta spectral triples. *arXiv preprint arXiv:2511.22755 [math.NT]*, 2025.
- [9] Alain Connes and Walter D. van Suijlekom. Quadratic forms, real zeros and echoes of the spectral action. *arXiv preprint arXiv:2511.23257 [math.OA]*, 2025.
- [10] E. B. Davies and M. Plum. Spectral pollution. *IMA Journal of Numerical Analysis*, 24(3):417–438, 2004.
- [11] Michael Levitin and Eugene Shargorodsky. Spectral pollution and second-order relative spectra for self-adjoint operators. *IMA Journal of Numerical Analysis*, 24(3):393–416, 2004.
- [12] Hugh L. Montgomery. The pair correlation of zeros of the zeta function. In Harold G. Diamond, editor, *Analytic Number Theory*, volume 24 of *Proceedings of Symposia in Pure Mathematics*, pages 181–193. American Mathematical Society, 1973.
- [13] Beresford N. Parlett. *The Symmetric Eigenvalue Problem*, volume 20 of *Classics in Applied Mathematics*. SIAM, Philadelphia, 1998.
- [14] Dominik Śliwiński. Spectral analysis of the $d_{\log}^{(\lambda, N)}$ operators. *arXiv preprint arXiv:2601.12133 [math.SP]*, 2026.

A Summary of Numerical Results

For reference, we collect the final precision-resolved measurements in a single table. All rows use $T = 800$, $N = 100$, $\text{dps} = 150$ ($c \leq 37$) or $\text{dps} = 200$ ($c \geq 41$).

Table 20: Complete 15-point results at $N = 100$, $T = 800$, $\text{dps} = 150$ ($c \leq 37$) / $\text{dps} = 200$ ($c \geq 41$).

c	$L = \log c$	$\lambda_{\min}^{\text{even}}$	$ \gamma_1 \text{ error} $	$ \gamma_1 \text{ err} /\lambda_{\min}$	$\log_{10} \gamma_1 \text{ err} $
13	2.565	2.865×10^{-59}	2.005×10^{-55}	6999	-54.70
14	2.639	4.835×10^{-65}	3.541×10^{-61}	7324	-60.45
17	2.833	2.030×10^{-80}	1.634×10^{-76}	8047	-75.79
19	2.944	1.265×10^{-90}	1.070×10^{-86}	8457	-85.97
23	3.135	5.959×10^{-107}	5.520×10^{-103}	9262	-102.26
29	3.367	4.366×10^{-124}	4.587×10^{-120}	10507	-119.34
31	3.434	1.045×10^{-128}	1.141×10^{-124}	10919	-123.94
37	3.611	4.670×10^{-140}	5.686×10^{-136}	12177	-135.25
41	3.714	2.122×10^{-146}	2.760×10^{-142}	13004	-141.56
43	3.761	2.519×10^{-149}	3.379×10^{-145}	13412	-144.47
47	3.850	2.994×10^{-154}	4.270×10^{-150}	14260	-149.37
53	3.970	9.615×10^{-161}	1.493×10^{-156}	15529	-155.83
59	4.078	2.328×10^{-166}	3.911×10^{-162}	16800	-161.41
61	4.111	5.063×10^{-168}	8.722×10^{-164}	17226	-163.06
67	4.205	7.993×10^{-173}	1.478×10^{-168}	18489	-167.83

The step sizes are non-uniform, ranging from -1.65 ($c = 59 \rightarrow 61$) to -17.08 ($c = 23 \rightarrow 29$). The $c = 13 \rightarrow 14$ step is notable: $c = 14$ is not prime, so no new prime enters the operator, yet the error improves by 5.8 OOM purely from the increase in interval length $L = \log c$. The variation in step sizes is strongly correlated with $\Delta L = \Delta \log c$ (Pearson $r = -0.96$). The normalized slope $\Delta \log_{10} |\text{error}|/\Delta L$ is far more uniform than the raw steps (coefficient of variation 0.17 vs 0.52).

B Pre-Registered Convergence Model Residuals

The original three models (M1–M3) were pre-registered and fit to 3-point $\text{dps} = 80$ data in Iteration 5; all failed with max residuals 2.44–2.68. Two additional models (M4, M5) were added for the 10-point sweep; three prime-counting models (M6–M8) were added for the 15-point dataset. A five-parameter log-periodic model was fit to the 10-point training data and tested out-of-sample at $c = 47$ and $c = 53$.

M5 (exponential-in- L) is the best-performing two-parameter model but still exceeds the ≤ 0.5 threshold by a factor of 3.5. M6–M8, which use prime-counting independent variables, perform substantially worse (max residuals 10–12), indicating that the convergence is not proportional to any standard prime-counting function.

The log-periodic model (5 parameters on 10 training points) achieved max residual 0.74 on training data — the first model to beat the ≤ 1.77 threshold. However, pre-registered blind predictions at $c = 47$ and $c = 53$ yielded residuals of 1.5 and 5.5 respectively: the model predicted that $c = 53$ would be *less* precise than $c = 47$, contradicting the observed monotone improvement. The model was overfitting noise in the training range. This clean out-of-sample falsification strengthens the negative result: no parametric model tested — including models with up to 5 free parameters

Table 21: Log-scale steps between consecutive cutoffs ($T = 800$).

Pair	$\Delta \log_{10} \gamma_1 \text{ error} $	New prime
$c = 13 \rightarrow 14$	-5.75	(none)
$c = 14 \rightarrow 17$	-15.34	17
$c = 17 \rightarrow 19$	-10.18	19
$c = 19 \rightarrow 23$	-16.29	23
$c = 23 \rightarrow 29$	-17.08	29
$c = 29 \rightarrow 31$	-4.60	31
$c = 31 \rightarrow 37$	-11.31	37
$c = 37 \rightarrow 41$	-6.31	41
$c = 41 \rightarrow 43$	-2.91	43
$c = 43 \rightarrow 47$	-4.90	47
$c = 47 \rightarrow 53$	-6.46	53
$c = 53 \rightarrow 59$	-5.58	59
$c = 59 \rightarrow 61$	-1.65	61
$c = 61 \rightarrow 67$	-4.77	67

Table 22: Full model-fit comparison: 15-point, 10-point, and 3-point residuals. All models use 2 free parameters except the log-periodic model (5 parameters).

Model	Form	Max res. (15-pt)	Max res. (10-pt)	Max res. (3-pt)
M1	$a \cdot L + b$	2.66	2.66	2.44
M2	$a \cdot L^2 + b$	4.71	4.71	2.68
M3	$a \cdot L \log L + b$	3.63	3.63	2.56
M4	$a \cdot L + b \cdot \log L$	2.66	2.66	—
M5	$a \cdot \exp(b \cdot L)$	1.77	1.77	—
M6	$a \cdot \pi(c) + b$	10.28	—	—
M7	$a \cdot \vartheta(c) + b$	12.09	—	—
M8	$a \cdot \#\text{pp}(c) + b$	10.20	—	—
<i>Higher-parameter models:</i>				
Log-periodic (5-param)	$a \cdot L + b + A \sin(\omega L + \phi)$	5.71	0.74	—

— captures the c -dependence of $|\gamma_1 \text{ error}|$.

C Reproducibility Discipline

This appendix collects the procedural rules enforced across the project’s iterations. These are reproducibility-hygiene practices, not mathematical claims; they are recorded here for transparency about how the numerical results in the body were produced and verified.

- **Pre-registration.** Each iteration’s experimental plan, including success/failure criteria and gate rules, is written and frozen before code execution.
- **Regression checking.** The $c = 13$ row is verified to all reported digits against the prior iteration’s result at each new iteration.
- **Banned-phrase discipline.** A cumulative list of banned phrases (including “validates,”

“confirms conjecture,” “proof,” “reached the mathematical limit”) is maintained and enforced across all writeups.

- **Adversarial review loop.** Each iteration undergoes a structured adversarial review during development.
- **Structured output.** All numerical results are stored in machine-readable JSON with full-precision strings. No result is reported from terminal output alone.